The Astrophysical Journal, 715:1282–1301, 2010 June 1 doi:10.1088/0004-637X/715/2/1282
© 2010. The American Astronomical Society. All rights reserved. Printed in the U.S.A.

MODELING OF GAMMA-RAY PULSAR LIGHT CURVES USING THE FORCE-FREE MAGNETIC FIELD

Xue-Ning Bai and Anatoly Spitkovsky
Department of Astrophysical Sciences, Princeton University, Princeton, NJ 08544, USA; xbai@astro.princeton.edu, anatoly@astro.princeton.edu
Received 2009 November 1; accepted 2010 April 17; published 2010 May 10

ABSTRACT

Gamma-ray emission from pulsars has long been modeled using a vacuum dipole field. This approximation ignores changes in the field structure caused by the magnetospheric plasma and strong plasma currents. We present the first results of gamma-ray pulsar light-curve modeling using the more realistic field taken from three-dimensional force-free (FF) magnetospheric simulations. Having the geometry of the field, we apply several prescriptions for the location of the emission zone, comparing the light curves to observations. We find that when the emission region is chosen according to the conventional slot-gap (or two-pole caustic) prescription, the model fails to produce double-peak pulse profiles, mainly because the size of the polar cap in the FF magnetosphere is larger than the vacuum field polar cap. This suppresses caustic formation in the inner magnetosphere. The conventional outer-gap model is capable of producing only one peak under general conditions because a large fraction of open field lines does not cross the null charge surface. We propose a novel "separatrix layer" model, where the high-energy emission originates from a thin layer on the open field lines just inside of the separatrix that bounds the open flux tube. The emission from this layer generates two strong caustics on the sky map due to the effect we term "Sky Map Stagnation" (SMS). It is related to the fact that the FF field asymptotically approaches the field of a rotating split monopole, and the photons emitted on such field lines in the outer magnetosphere arrive to the observer in phase. The double-peak light curve is a natural consequence of SMS. We show that most features of the currently available gamma-ray pulsar light curves can be reasonably well reproduced and explained with the separatrix layer model using the FF field. Association of the emission region with the current sheet will guide more detailed future studies of the magnetospheric acceleration physics.

Key words: gamma rays: general – magnetohydrodynamics (MHD) – pulsars: general – stars: magnetic field

Online-only material: color figures, animation

1. INTRODUCTION

Gamma-ray pulsars are of great scientific interest in high-energy astrophysics. The high-energy emission from these objects provides valuable information about pulsar magnetospheric structure, particle acceleration mechanisms, and plasma physics in strong magnetic fields. Observations by the Energetic Gamma Ray Experiment Telescope (EGRET) onboard *Compton Gamma Ray Observatory* (*CGRO*) confirmed seven gamma-ray pulsars (Thompson 2004). The light curves of these pulsars are characterized by widely separated double-peak features, with the first peak typically lagging the radio pulse by a small fraction of rotation period. Recently, the *AGILE* mission has detected several new gamma-ray pulsars and refined the detection of some previously known pulsars (Halpern et al. 2008; Pellizzoni et al. 2009a, 2009b). More impressively, one year after launch, the Large Area Telescope (LAT) onboard *Fermi Gamma-ray Space Telescope* (*Fermi*) has discovered more than 40 new gamma-ray pulsars (Abdo et al. 2008, 2009a, 2009c, 2009f, 2009g, 2010). The sensitivity and timing capability of *Fermi*–LAT have also provided the most precise light curves and phase resolved pulsar spectra (Abdo et al. 2009b, 2009d, 2009e). These new discoveries have greatly expanded the sample of gamma-ray pulsars and underscored the importance of understanding the origin of double-peak profiles. At the same time, the diversity of light curves from the latest gamma-ray pulsar samples calls for improvements in theoretical modeling.

The widely separated double peak feature in the gamma-ray light curves suggests emission coming from the outer magnetosphere. Gamma rays are believed to be produced by energetic particles accelerated in the "gap" regions in the magnetosphere. The particles emit via curvature, synchrotron, and inverse Compton (IC) radiation. Various theoretical models differ in the assumed location of the emission zones (i.e., the gaps). Conventional models for pulsar gamma-ray emission include the polar cap model (Harding et al. 1978; Daugherty & Harding 1982, 1996), the slot gap model (SG, or two-pole caustic model, TPC for short; Arons & Scharlemann 1979; Arons 1983; Muslimov & Harding 2003, 2004; Dyks & Rudak 2003; Dyks et al. 2004), the outer gap model (OG; Cheng et al. 1986a, 1986b; Romani & Yadigaroglu 1995; Yadigaroglu 1997; Cheng et al. 2000), as well as the inner annular gap model (IAG; Qiao et al. 2004, 2007).

Most calculations from these models approximate the pulsar magnetosphere by a rotating magnetic dipole field. In reality, the magnetosphere is known to be filled with plasma (Goldreich & Julian 1969). This plasma is essentially force-free (FF), satisfying $\rho \boldsymbol{E} + \boldsymbol{j} \times \boldsymbol{B}/c = 0$, where ρ and $\boldsymbol{j}$ are the charge and current densities. The structure of the FF magnetosphere differs substantially from the rotating dipole field due to the poloidal current and the returning current sheet (Contopoulos et al. 1999; Gruzinov 2005; Komissarov 2006; McKinney 2006; Timokhin 2006). Recently, FF magnetospheric field structure in three dimensions (3D) has become available from the time-dependent FF simulations (Spitkovsky 2006; Kalapotharakos & Contopoulos 2010). The FF magnetosphere satisfies $\boldsymbol{E} \cdot \boldsymbol{B} = 0$ everywhere; hence, no particle acceleration or emission can formally occur. Real pulsars must lie somewhere between the vacuum, which has $\boldsymbol{E} \cdot \boldsymbol{B} \neq 0$ everywhere, and FF cases. The fact that the power of gamma-ray emission is a small, though non-negligible ($\lesssim$20%), fraction of the total spin down power suggests that FF should be a reasonable approximation to the

overall field structure with the exception of relatively small regions where acceleration takes place.

In the companion paper (Bai & Spitkovsky 2010, hereafter BS10), we demonstrated that the modeling of gamma-ray pulsar light curves using the vacuum dipole field is subject to large uncertainties. This is because the peaks in the vacuum light curve are caused by the fortuitous overlap of radiation from different regions of the magnetosphere (caustics). This overlap is sensitive to the geometry of the magnetic field due to two effects. First, the shape of the field controls how the aberration of light and light travel delay add together to cause the formation of caustics. We showed that a seemingly small change of treating the retarded vacuum field in the instantaneously corotating frame, rather than in the laboratory frame where it should be defined, can lead to significant reduction in the strength of caustics in the TPC/SG and to the moderate dilution of the OG peaks. Second, the behavior of the field near the light cylinder (LC) determines the shape of the polar cap on the star, and, hence, indirectly controls the shape of the emission zone, even if it is located in the inner magnetosphere. We considered the sensitivity of the caustic formation to the modification of shape of the vacuum polar cap. We compared the polar cap obtained by tracing the vacuum field lines to a simple circular polar cap. This change significantly affected the caustics of the TPC model. The OG model was less sensitive to this change, but, since the emission zone for the OG is in the outer magnetosphere, the field shape there is likely to be strongly modified by the inclusion of plasma effects. Given these uncertainties in the vacuum field modeling, it is highly desirable to revisit the existing models using the FF field configuration and compare the results with the latest observations.

In this paper, we use the FF field from 3D time-dependent simulations by Spitkovsky (2006, hereafter S06) and present the calculation of pulsar gamma-ray light curves using various theoretical models of emission. In Section 2, we provide the general analysis of FF field structure, addressing the location of the current sheet and its association with magnetic field lines. In Section 3, we describe our numerical method and theoretical models for calculating the gamma-ray light curves. Sections 4–6 are dedicated to comparison between different models. We show in Section 4 that the conventional TPC model fails to produce double-peak light curves using the FF field. We propose a novel "separatrix layer" (SL) model in Section 5, in which the emission zone is fixed in a layer just inside the separatrix associated with the strong current sheet. This layer can be accurately traced by open field lines originating in an annulus just inside the polar cap rim.[1] This model differs from the conventional TPC model in that the emission zone is not concentrated on the last open field lines, but rather interior to them, and it spans a larger range of heights up to and beyond the LC. It differs from the conventional OG model in that the emission zone consists of all field lines in a given flux tube, and not just those that cross the null charge surface (NCS). The double-peak light curve is a generic property of the FF field structure, where caustics of emission form in the outer magnetosphere when the field lines approach the split-monopolar geometry. We call this "the stagnation effect" on the sky map. In Section 6, we show that the conventional OG model applied to the FF field has difficulty in producing double-peak light curves unless a carefully chosen inclination angle and viewing geometry are used. We discuss various implications of our results to the pulsar acceleration mechanisms and compare our results with recent observations in Section 7. The main results are summarized in Section 8.

[1] In the original version of this paper, we termed this model the "annular gap" model. The name "separatrix layer" more accurately describes the location of the emission zone and avoids the confusion with the "inner annular gap" model (Qiao et al. 2004). Moreover, although this paper is based only on geometry, the association of the emission layer with the magnetospheric current sheet (see Section 7.2) implies that the acceleration may not necessarily involve a "gap" at all.

2. STRUCTURE OF THE FORCE-FREE MAGNETOSPHERE

Force-free pulsar simulations evolve a rotating magnetized conducting sphere immersed in a massless infinitely conducting fluid. The simulations are 3D and start with an inclined dipolar field attached to a sphere (S06). The resolution of our simulations is 80 cells per LC radius, $R_{\rm LC} = c/\Omega$, and the radius of the star in simulations is 15 cells ($R_N^{\rm sim} \sim 0.19 R_{\rm LC}$). We ran a series of simulations varying the inclination angle between the pulsar's magnetic and rotation axes from $\alpha = 0^\circ$ to $\alpha = 90^\circ$ with an interval of 15°. The FF fields are extracted after evolving the FF equations for 1.2 stellar rotations. Evolving for longer times makes little difference to the field structure (Kalapotharakos & Contopoulos 2010). In Section 2.1, we illustrate the charge density and current structure of the FF field, and present the properties of the FF polar cap in Section 2.2. The 3D current sheet structure of the FF field is discussed in Section 2.3.

2.1. Charge and Current in the Force-free Field

While it is not possible to determine individually the density and velocity of positively and negatively charged particles solely from the FF model, the FF current and charge density contain rich physical information from which we can gain useful insights.

In ideal FF electrodynamics, by assuming that electromagnetic field pattern corotates with the pulsar, we obtain (Gruzinov 2006)

$$\boldsymbol{E} = -\vec{\beta}_0 \times \boldsymbol{B}, \tag{1}$$

$$\nabla \times [\boldsymbol{B} + \vec{\beta}_0 \times (\vec{\beta}_0 \times \boldsymbol{B})] = \lambda \boldsymbol{B}, \tag{2}$$

where $\vec{\beta}_0 \equiv \times \boldsymbol{r}/c$ is the normalized corotation velocity and λ is a scalar function that is conserved along the magnetic field lines because $\boldsymbol{B} \cdot \nabla\lambda = 0$. In the case of the aligned rotator, parameter λ is the analog of $A'(\Psi)$ in the pulsar equation (Michel 1973a, 1973b), where A is proportional to the poloidal current, and the derivative is with respect to the poloidal magnetic flux Ψ. Therefore, $\lambda \propto A'$ characterizes the current per magnetic flux. More specifically, positive λ represents current along the magnetic field line, while negative λ represents current flow opposite to the direction of the magnetic field. A formal derivation for the physical meaning of λ can be found in Appendix A, where we show that $\lambda \boldsymbol{B}$ is the field-aligned current density in the CF. We calculate λ by taking the dot product of $\boldsymbol{B}/B^2$ on both sides of Equation (2).

In Figure 1, we show the color plots of λ in the Ω–μ plane (the plane containing the rotation axis and the magnetic moment vector) for a range of inclination angles. We also show vectors of the magnetic field projected onto this plane. The strong current layer manifests itself as a local enhancement of λ. First, consider the axisymmetric pulsar magnetosphere ($\alpha = 0$). The field structure closely resembles the solution by Timokhin (2006)

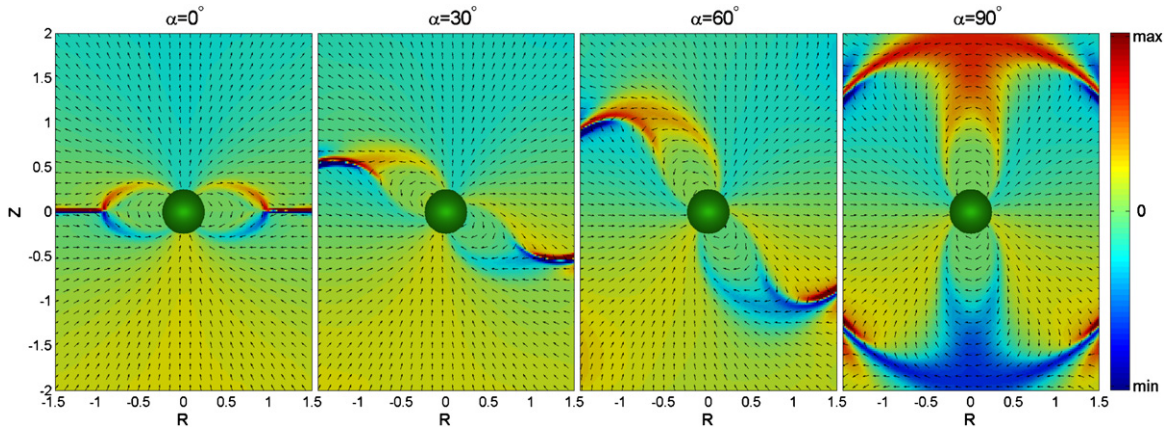

Figure 1. Color plots of the parameter λ of the FF field in the Ω–μ plane for magnetic inclination angles $\alpha = 0°, 30°, 60°$, and 90° respectively. Arrows show the direction of the projected magnetic field in this plane. All plots have units in LC radius R_{LC} and have the same color scale.

(A color version of this figure is available in the online journal.)

with $x_0 \equiv R_Y/R_{LC} \lesssim 1$ and well approaches the CKF solution[2] (Contopoulos et al. 1999). In agreement with these solutions, the current along the open field lines in our simulation is predominantly of one sign in each hemisphere; however, near the edge of the open zone there is a distributed return current region bounded by a strong return current sheet. Instead of a delta-function current sheet expected in theory, the simulation current sheet is several grid cells thick, giving λ a finite maximum/minimum there. The open field lines increasingly resemble the rotating split monopole solution beyond the LC and become radial in the poloidal section. The left panel of Figure 1 illustrates these features.

Next, consider the general oblique rotators. The transition of current structure is smooth as α increases from 0° to 90°. In Figure 1, we see that at small inclination angle, $\alpha = 30°$, the pattern of λ is similar to the axisymmetric case, and the current sheet inside the LC appears slightly wider and weaker. As the inclination angle increases, there are also current sheet-like features inside the LC, but the distribution of current becomes very asymmetric, and more current is returned to the polar cap through the distributed flow rather than the current sheet. The current flow in the polar cap is predominantly of one sign (e.g., ingoing) for the aligned rotator, bounded by a strong current sheet of opposite sign (e.g., outgoing), and is symmetric with respect to the equatorial plane. In contrast, when $\alpha = 90°$, the current flow has different signs in the northern and southern halves of the polar cap (this can be better seen in Figure 4, which shows the current through the polar cap, see Section 2.2), and the current distribution is anti-symmetric with respect to the equatorial plane. On the periphery of the polar cap there are thin current layers, as shown in red (upper) and blue (lower) oval structures in the right panel of Figure 1. The current in these current layers forms loops connecting the two poles through the closed zone. Integrating over the polar cap, we find that the amount of current flowing to the other pole is about 20% of the current flowing on open field lines. Such closed current loops for orthogonal rotators are qualitatively consistent with predictions of the model by Gurevich et al. (1993), although we find the amount of current shunting to the other pole to be smaller in our simulations. The total current on the open field lines (integrated by magnitude) is just 20% smaller for the orthogonal rotator than for the aligned rotator, suggesting that the current density for the orthogonal rotator exceeds the simple expectation of the speed of light times local Goldreich–Julian (GJ) density on the polar cap. This current cannot be provided by charge-separated flow alone and requires abundant pair formation. The details of the current adjustment in such polar caps are still uncertain (Lyubarsky 2009).

A thin current sheet *outside* the LC exists for all inclination angles; its structure asymptotically approaches the rotating split monopole solution outlined by Bogovalov (1999). If the current sheet outside the LC is connected to the star, it must be connected through a current sheet inside the LC because the current flow in the CF cannot cross magnetic field lines, as inferred from Equation (A6). In Appendix B, we show that the amount of current in the current sheet outside the LC that is connected to the star monotonically decreases with inclination angle. This is related to the degradation of the current sheet *inside* the LC and the thickening of the *Y*-region for oblique rotators shown in Figure 1. These features are unlikely to be caused by numerical resistivity, and we have tested that the thickness of the *Y*-region and the strong current layers inside the LC is not sensitive to numerical resolution. For the orthogonal rotator, the current sheet outside the LC is totally disconnected from the star (see Appendix B). Therefore, the oval structures in the right panel of Figure 1 are most likely the current loops that connect the two poles, rather than current sheets connecting to the outer magnetosphere. This strongly contrasts with the case of the aligned rotator, where the current sheet inside the LC unambiguously exists and connects to the equatorial current sheet outside the LC. While there are definitely strong currents flowing on the periphery of the open field lines for all other inclinations seen from Figure 1, determining whether their thickness is finite or infinitesimal would require further study (see Section 2.2 for a speculative discussion). Throughout this paper, we will refer to these current sheet-like features inside the LC as "strong current layers."

The charge density necessary to provide corotation of the magnetosphere is referred to as GJ charge density (Goldreich &

[2] In our simulation, the numerical resistivity is very low when the equatorial current sheet is aligned with the grid. Therefore, for inclination angles <10° the evolution of the *Y*-point to the LC takes longer than 2 turns to approach the expected result (S06). Larger inclination angles are well converged by 1.2 turns. We have checked this convergence by comparing results between 1.2 turns and 2 turns (where we manage to avoid reflection by using a very large computational domain). No significant difference is found for $\alpha > 15°$. In Figures 1–4, however, we do show the field structure after 2 turns, to allow the *Y*-point in the $\alpha = 0°$ case to get closer to the LC.

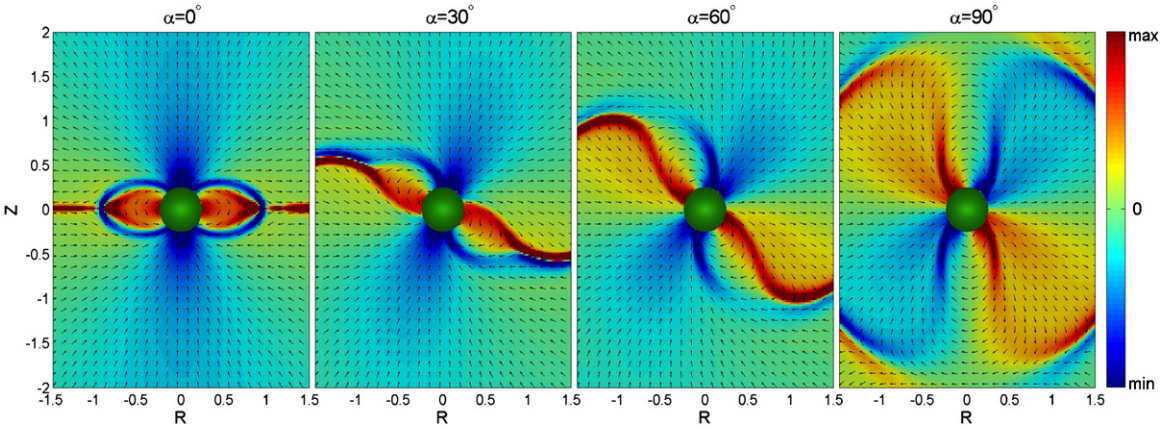

Figure 2. Color plots of the charge density ρ in the FF field in the Ω–μ plane for magnetic inclination angles $\alpha = 0°$, 30°, 60°, and 90°. We have multiplied ρ by r^2 to improve the contrast. Arrows indicate the direction of the projected magnetic field in this plane. All plots have units in LC radius $R_{\rm LC}$ and have the same color scale. (A color version of this figure is available in the online journal.)

Julian 1969). It can be written as

$$\rho = \frac{\nabla \cdot \boldsymbol{E}}{4\pi} = -\frac{\boldsymbol{\Omega} \cdot \boldsymbol{B}}{2\pi c} + \frac{\vec{\beta}_0 \cdot (\nabla \times \boldsymbol{B})}{4\pi}. \quad (3)$$

If we assume complete charge separation, as in Goldreich & Julian (1969), then the second term is of the order $\rho\beta_0^2$, and we arrive at the classical result with $\rho \propto \boldsymbol{\Omega} \cdot \boldsymbol{B}$. Whether a real pulsar magnetosphere has complete charge separation is not clear, but the eclipse in the double pulsar system PSR J0737−3039 indicates that the particle density in the inner magnetosphere is much higher than typical GJ density (Rafikov & Goldreich 2005; Lyutikov & Thompson 2005). In Figure 2, we plot the charge density from the FF simulation. We find that the bulk distribution of FF charge density is approximately proportional to $\boldsymbol{\Omega} \cdot \boldsymbol{B}$. However, there is a significant enhancement of charge density in the strong current layer and in the current sheet beyond the LC, which is due to the contribution of the current in the second term of Equation (3).

The distribution of charge in the strong current layer inside the LC has another notable feature. In Figure 2, the charge distribution is symmetric between the north and south magnetic hemispheres for the aligned rotator. Dense negative charges more or less uniformly fill the current sheet inside the *Y*-point, while the current sheet outside the *Y*-point is positively charged (Timokhin 2006). However, this symmetry is broken when α is different from zero (e.g., at $\alpha = 30°$). The strong current layer inside the LC then contains both signs of charge, with the northern and southern parts having opposite signs at fixed azimuth. The current sheet outside the LC also contains charges of both signs, although one sign of charge is prevailing (in red color). This trend is also observed by Contopoulos & Kalapotharakos (2010).

It is also useful to visualize the FF magnetosphere in terms of space-like and time-like regions of 4-current. A 4-current is space-like if $\boldsymbol{j}^2 - \rho^2 > 0$; otherwise, it is time-like. Note that this definition is Lorentz invariant. Regions with space-like current demand counter-streaming of different signs of charge in the frame where $\rho = 0$. This could lead to plasma instabilities and dissipation (Lyubarskii 1996; Gruzinov 2007b). A current sheet with space-like current could then be expected to produce particle acceleration and gamma-rays (Gruzinov 2007a; Lyubarsky 2008; Spitkovsky 2008). In the asymptotic split-monopole regime of Bogovalov (1999), one expects the current sheet outside the LC to be space-like. This is because both magnetic and electric fields change sign across the current sheet, and since $|\boldsymbol{B}| > |\boldsymbol{E}|$ outside the current sheet, MHD jump condition demands $J > \sigma c$ in the current sheet, where J and σ are surface current and surface charge densities.[3] In Figure 3, we plot the Lorentz invariant quantity

$$\varrho \equiv \pm\sqrt{|\rho^2 c^2 - \boldsymbol{j}^2|}, \quad (4)$$

where we take the plus sign for time-like current and the minus sign for space-like current; thus, counter-streaming is required in the regions which are negative. We find that in both aligned and oblique rotators the current sheet outside the LC is in general space-like (blue). Although there are regions in red around the current sheet, the overall surface integrated ϱ is negative, as expected. The strong current layer inside the LC appears to be predominantly time-like. The magnetosphere in the aligned rotator is dominated by time-like regions, and only in regions near the NCS does it show very small negative values of ϱ. As the inclination angle increases, the space-like region becomes much broader, occupying a substantial fraction of the open field-line regions. We will discuss this further in Section 7.

2.2. The Force-free Polar Cap

The polar cap is the region on the neutron star (NS) surface where open magnetic field lines originate. The rim of the polar cap is set by the locus of last open field lines (LOFLs). We adopt the conventional definition of LOFLs, where we treat a field line as open if it crosses the LC; otherwise, it is regarded as closed. This is an oversimplification, as in the FF field the closed zone does not have to extend to the LC everywhere; some closed field lines may also extend through the LC and close through the current sheet. However, this simple definition facilitates comparison with calculations using the vacuum field.[4] In Figure 4, we plot the shape of the FF polar cap on the sphere

[3] We thank Yuri Lyubarsky for pointing this out to us.

[4] Moreover, it is probably better not to distinguish between open and closed field lines, but to distinguish between "active" and "dead" field lines. Dead field lines are closed within the *Y*-point, beyond which the equatorial current sheet is launched. Other field lines, including open field lines and field lines that are closed through the current sheet, are considered active. Therefore, one may consider "last active field lines" as a more meaningful concept in the FF magnetosphere. Our definition of last open field lines as active field lines is equivalent to setting the radius of the *Y*-point to be at the light cylinder.

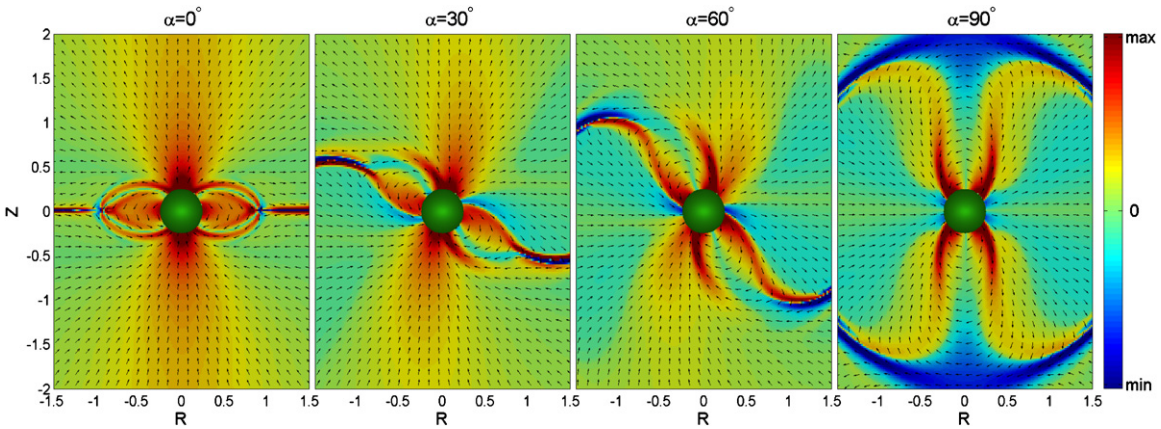

Figure 3. Color plots of the parameter ϱ (see Equation (4)) of the FF field in the Ω–B plane for a magnetic inclination angle $\alpha = 0°, 30°, 60°$, and $90°$. We have multiplied ϱ by r^2 to improve the contrast. Arrows show the direction of the projected magnetic field in this plane. All plots have units in LC radius $R_{\rm LC}$ and have the same color scale.

(A color version of this figure is available in the online journal.)

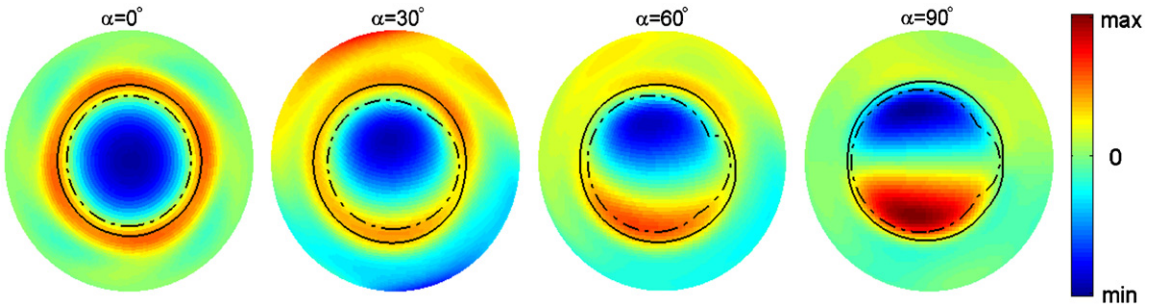

Figure 4. Shape of the polar caps in FF field (solid lines) and the Deutsch field (dash-dotted lines) for magnetic inclination angles $\alpha = 0°, 30°, 60°$, and $90°$ (left to right). Overlaid are the color plots of the current to flux ratio λ on the pulsar surface. To better visualize λ, the size of the pulsar is set to be $0.25R_{\rm LC}$. Also, the color scale of λ is compressed compared to Figure 1.

(A color version of this figure is available in the online journal.)

of radius $0.25R_{\rm LC}$ for inclination angles $\alpha = 0°, 30°, 60°, 90°$. The surface of the sphere (which is larger than the NS for ease of visualization) is colored with the parameter λ, indicating the sense of the current flow. For comparison, we also plot with dash-dotted lines the polar caps obtained from the retarded vacuum magnetic dipole field (Deutsch 1955). We note that tracing vacuum field lines beyond the LC always returns them back to the star because vacuum solution does not have the current sheet. Nevertheless, as is conventional in the literature, we always call vacuum field lines that go beyond the LC "open," although they are still formally closed.

From Figure 4 we see that the polar cap of the FF field encloses the current flowing into and out of the pulsar. The polar current switches from flowing into the NS at $\alpha = 0°$, to equal halves of oppositely directed current at $\alpha = 90°$. The peak of the current density slightly lags the zero phase (i.e., the phase of the magnetic pole) due to pulsar rotation. The evolution of the strong current layer as α increases can also be clearly seen from Figure 4. For the aligned rotator, the rim of the polar cap corresponds to the footprint of the current sheet (i.e., the red enhancement on the left panel), as expected. As α increases, the strong current thickens on one side (lower side in Figure 4) and weakens on the other side. The thickened part may no longer count as a current sheet, as it gradually occupies half of the polar cap to become the main contributor of the polar current at $\alpha = 90°$. The weakened side gradually shifts to the outside of the polar cap (at $\alpha = 90°$), and forms the current loop in the closed field lines as seen in the rightmost panel of Figure 1. Following the discussion in the previous subsection, we speculate that the weakened part of the strong current layer actually corresponds to the current sheet inside the LC. The current sheet covers a circle on the polar cap for the aligned rotator. For oblique rotators, the region covered by the current sheet on the polar cap reduces to an arc covering the upper part of the polar cap in Figure 4. The extent of the arc-like region shrinks with inclination angle α, consistent with the reduction of star-connecting current in the current sheet *outside* the LC. In the meantime, some current in the arc-like region on the polar cap becomes connected to the other pole, forming current loops. This is associated with the thickening of the *Y*-region discussed in the previous subsection. The loop current is zero for the aligned rotator and increases to about 20% of the total polar current for the orthogonal rotator.

We note that the FF polar caps are smooth and approximately circular. On the other hand, polar caps obtained from oblique vacuum dipole rotators display notch structures and sharp jumps (Dyks et al. 2004). As was shown in BS10, gamma-ray light curves are sensitive to the shape of the polar caps, as this changes the formation of caustics in the emission. The FF polar cap is also larger than its vacuum counterpart, due to the larger open magnetic flux. This is consistent with the larger spin down power for the FF rotator compared to the equivalent vacuum rotator (S06). The same effect is seen in the aligned rotator (Contopoulos et al. 1999). As a result, the LOFLs predicted from the vacuum dipole field should lie within the LOFLs, or in the open volume, of the FF field. This effect

also has significant consequences to the appearance of the FF sky map.

The magnetic field lines that originate near the polar cap from the NS surface can be parameterized using the open volume coordinate system (Yadigaroglu 1997; Cheng et al. 2000; Dyks et al. 2004). This system has two coordinates, (r_{ov}, ϕ_m), recording the footprint on the NS surface, where ϕ_m is the magnetic azimuth, and r_{ov} is the magnetic colatitude normalized by the magnetic colatitude of the LOFLs. Therefore, the LOFLs correspond to $r_{ov} = 1$, and open field lines have $r_{ov} < 1$.

2.3. Current Sheet–Field Line Association

Current sheets are generic features of FF pulsar magnetosphere. To better visualize the current sheet structure, we present a volume rendering plot in Figure 5, showing the magnitude of the current function λ as volume opacity and two sets of flux tubes ($r_{ov} = 1$ and 0.9) as color lines. This figure demonstrates the relation between regions of strong current and magnetic field lines for $\alpha = 60^\circ$ rotator.

First of all, we see that LOFLs are associated with the strong current layer inside the LC. Note that the current layer has finite thickness, and it encloses the LOFLs. Some field lines with $r_{ov} < 1.0$ and $r_{ov} > 1.0$ also lie within the strong current layer. Moreover, due to magnetic reconnection in the current sheet (outside the LC), field lines can be closed beyond the LC, and we observe that some outgoing field lines with $r_{ov} \gtrsim 0.95$ stall and turn inward beyond the LC. These field lines trace the current sheet outside the LC to a finite distance before turning back. This effect makes finding the true LOFLs a more complicated exercise than we perform in this paper.

Second, we see that field lines with $r_{ov} \lesssim 0.95$ are generally open in the physical sense. The red curves in Figure 5 show some representative field lines with $r_{ov} = 0.90$. These field lines lie at the edge of the strong current layer inside the LC and follow closely the current sheet outside the LC. The current sheet outside the LC separates field lines originating from different poles.

We conclude that r_{ov} is a good tracer of current in the FF magnetosphere. For $\alpha = 60^\circ$ rotator, strong current is associated with $0.95 \lesssim r_{ov} \lesssim 1.05$, and field lines with $r_{ov} \lesssim 0.95$ lie outside the current sheet. For other inclination angles, the critical value of $r_{ov} = 0.95$ varies, but not significantly.

3. EMISSION CALCULATION

The FF magnetosphere has no intrinsic acceleration and emission since the condition $\boldsymbol{E} \cdot \boldsymbol{B} = 0$ is satisfied everywhere by construction. Therefore, we will calculate the pulsar gamma-ray emission based solely on geometric grounds. Specifically, the calculation involves a prescription of the emission zone and a method to determine the intensity and direction of emission inside the emission zone.

3.1. Emission Zone Geometry

Here we summarize the emission zone geometry prescriptions by different theoretical models that we consider in this paper.

The two-pole caustic (TPC) model is an extended version of the slot-gap (SG) model (e.g., Arons 1983). In this model, the emission is assumed to originate on LOFLs (i.e., $r_{ov} = 1$) from the NS surface up to some cutoff radius (Dyks & Rudak 2003; Dyks et al. 2004). We use two cutoff radii: spherical radius r_{max}, measured from the center of the NS, and cylindrical radius R_{max},

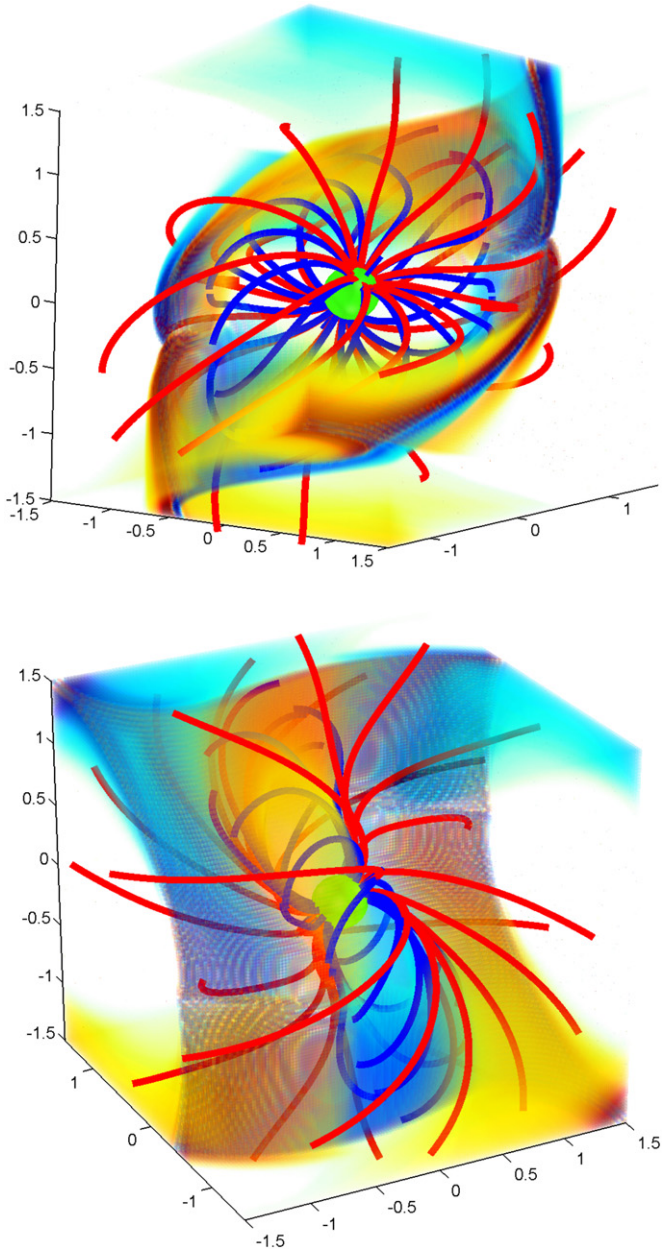

Figure 5. 3D volume rendering of the current to flux ratio λ, defined in Equation (2), for the FF simulation with $\alpha = 60^\circ$. Transparency is determined by $|\lambda|$, where only regions with large $|\lambda|$ are opaque. The color scale is the same as in Figure 1. Blue curves indicate the LOFLs, while the red curves are field lines with $r_{ov} = 0.90$. The two panels show different viewing angles. Axes are in units of R_{LC}. The movie version of this plot is available in the online version of the paper.

(An animation and a color version of this figure are available in the online journal.)

measured from the rotation axis. Together, these two parameters define the extent of the TPC emission zone.

In this paper, we also propose a new emission model which we term the separatrix layer (SL) model. In this model, we assume that emission comes from a layer in the vicinity of the separatrix, which separates open and closed field lines as well as field lines with different polaralities. As we have seen in Section 2.3, the location of the separatrix corresponds to strong current layer/current sheet. This SL is described by $r_{ov} \simeq 0.90$–0.95, going from the stellar surface up to a cutoff radius in a way that is similar to the TPC model. The cutoff radii for the SL model are

not limited to be inside the LC. We will discuss the physical justification for this model in Section 7.

For the outer gap (OG) model, the emission is assumed to originate on the open field lines beyond the NCS, and extends up to the LC. Recent refinements of the OG models allow the inner boundary of the gamma-ray emission to be inside the NCS (Hirotani 2007; Takata & Chang 2007; Takata et al. 2007, 2008). In order to incorporate such possibility, we assume that the emission comes from all field lines in a given flux tube that cross the NCS, extending from the stellar surface to certain cutoff radius. This approach maximizes the volume of the emission zone. The emission from the OG model is often assumed to be centered at certain $r_{\rm ov}$ (e.g., $r_{\rm ov} = 0.90$).

Unlike the OG model, the inner annular gap (IAG) model assumes that particles are accelerated in an annular open field line region extending from the NS surface to the NCS (Qiao et al. 2004, 2007). The emission zone is bounded by LOFLs and the critical field lines, which cross the LC at the NCS. To simplify, we may also think of emission from the IAG to be centered at certain $r_{\rm ov} < 1$.

For all models mentioned above, we consider the emission originating from annular regions centered at fixed $r_{\rm ov}$ with a Gaussian width $\Delta r_{\rm ov} = 0.025$ similar to Dyks et al. (2004) as our standard emission zone prescription. The radial extent of the emission zone is controlled by the location of the NCS (for OG and IAG models), as well as the $R_{\rm max}$ parameter (we do not use $r_{\rm max}$ in this paper).

3.2. Calculation Method

In calculating the gamma-ray light curves we adopt two basic assumptions. First, we assume that the emission is produced by outgoing energetic particles in the emission zone. These particles are confined to travel almost along the magnetic field line, but may acquire some pitch angle θ_p. Such pitch angle is expected from both conventional SG and OG models, e.g., acquired during the pair creation process (Tang et al. 2008), or via the cyclotron resonant absorption (Harding et al. 2008). If emission originates from the current sheet, as we postulate in Section 7.2, we would expect even larger pitch angles since in the current sheet, the magnetic field is relatively weak while the plasma is likely to be hot due to reconnection. The emission mechanism can involve synchrotron, curvature, and IC, but the direction of the emitted photon is along the direction of particle motion due to relativistic beaming. Calculation of the direction of emitted photon in the lab frame (LF), including the aberration and time delay effects, is discussed in detail in BS10. Here, we generalize these results to incorporate the effect of finite particle pitch angle. Consider a drift frame (DF) in which the electric field vanishes. Let the velocity of the DF relative to the LF be $\boldsymbol{V}_d$ and $\vec{\beta}_d = \boldsymbol{V}_d/c$. In this frame, let θ_p be the particle pitch angle. Then the emission direction is determined by

$$\boldsymbol{e} = (\alpha \cos\theta_p)\boldsymbol{t} + (\alpha \sin\theta_p \cos\varphi)\boldsymbol{n} + (\alpha \sin\theta_p \sin\varphi)\boldsymbol{b} + \vec{\beta}_d, \quad (5)$$

where $\boldsymbol{t}$, $\boldsymbol{n}$, and $\boldsymbol{b}$ are the tangential, normal, and binormal unit vectors to the magnetic field line (in the LF), and α is determined by requiring that $|\boldsymbol{e}| = 1$.

This formula is essentially the same as Equation (6) of Takata et al. (2007), except that it applies in any DF. The drift velocity can be chosen to be either the corotation velocity $\vec{\beta}_0$, or the $\boldsymbol{E} \times \boldsymbol{B}$ drift velocity. When $\theta_p = 0$, Equation (1) ensures that these two choices produce the same result. However, this is no longer the case for a finite pitch angle. This is because the pitch angle is not Lorentz invariant and depends on frames. Moreover, the DF velocity with $\vec{\beta}_d = \vec{\beta}_0$ is no longer valid at $R > R_{\rm LC}$ since the frame velocity becomes superluminal. Therefore, a better choice is to use the $\boldsymbol{E} \times \boldsymbol{B}$ drift velocity, which is the minimum drift velocity among all DFs, and this is the drift velocity we adopt throughout this paper. In our calculation, we further assume that the pitch angle is constant for all particles in the emission zone.

Our second assumption is constant emissivity along particle trajectories in the emission zone. In reality, as long as the particle emissivity does not vary dramatically in the emission zone, our calculation will be able to catch the overall features of gamma-ray light curves. Moreover, as pointed out in BS10, the overall appearance of the emission sky map is more sensitive to field structure than to emissivity, because the formation of caustics largely depends on the details of field configuration. Adopting constant particle emissivity will help us locate possible emission zones in the FF field by comparing with observations. For example, comparing model light curves with observations can help identify the radial extent of the emission zone (i.e., $R_{\rm max}$, see Section 5), which then places constraints on the physics of the radiation mechanism.

One basic difference in our approach compared to the previous work (e.g., Yadigaroglu 1997; Cheng et al. 2000; Dyks et al. 2004; Takata & Chang 2007; Harding et al. 2008; Watters et al. 2009) is that the emission is weighted by the length along particle trajectories rather than along magnetic field lines. We have discussed in BS10 that particle trajectory follows magnetic field lines in the CF, and the magnetic field in the CF is the same as the LF magnetic field. Therefore, to calculate particle trajectories, we trace magnetic field lines in the LF and add the effect of stellar rotation. In Appendix C, we provide a simple relation between segment length along a magnetic field line and along the corresponding particle trajectory. The difference is small well inside the LC, but the correction becomes important near the LC and beyond. Since the FF field does not break down at the LC, we will allow the emission zone to extend beyond the LC, where such correction is necessary.[5]

Finally, in our calculation photons from the emission zone are projected to the sky map $(\phi, \xi_{\rm obs})$, where ϕ corresponds to the rotation phase, and $\xi_{\rm obs}$ denotes the observer's viewing angle. A time delay correction is applied during the projection as usual

$$\phi = -\phi_e - \boldsymbol{r} \cdot \boldsymbol{e}/R_{\rm LC}. \quad (6)$$

The brightness of the sky map is proportional to the number of photons projected to the sky map bins, divided by the solid angle of each bin. The solid angle of each sky map bin is $d\Omega = \sin\xi_{\rm obs} d\xi_{\rm obs} d\phi$; therefore, the sky map brightness is proportional to photon counts in each bin divided by $\sin\xi_{\rm obs}$. Cutting the sky map at $\xi_{\rm obs}$ produces the light curve seen by the observer. The correction of $1/\sin\xi_{\rm obs}$ only affects the normalization of the light curves at each observer viewing angle, but not the shape of the light curves. Including it is important for the calculation of the flux correction factor used to infer the intrinsic luminosity of gamma-ray pulsars.

4. THE TWO-POLE CAUSTIC MODEL

In this section, we consider the emission from the TPC model ($r_{\rm ov} = 1.0$) in the FF field. The 3D shape of the LOFLs and the

[5] For example, consider a rotating split monopole field, where particle trajectories are straight lines, while the field lines are spirals. The FF field asymptotically approaches the split monopole field, and such correction avoids overweighing far-field emission.

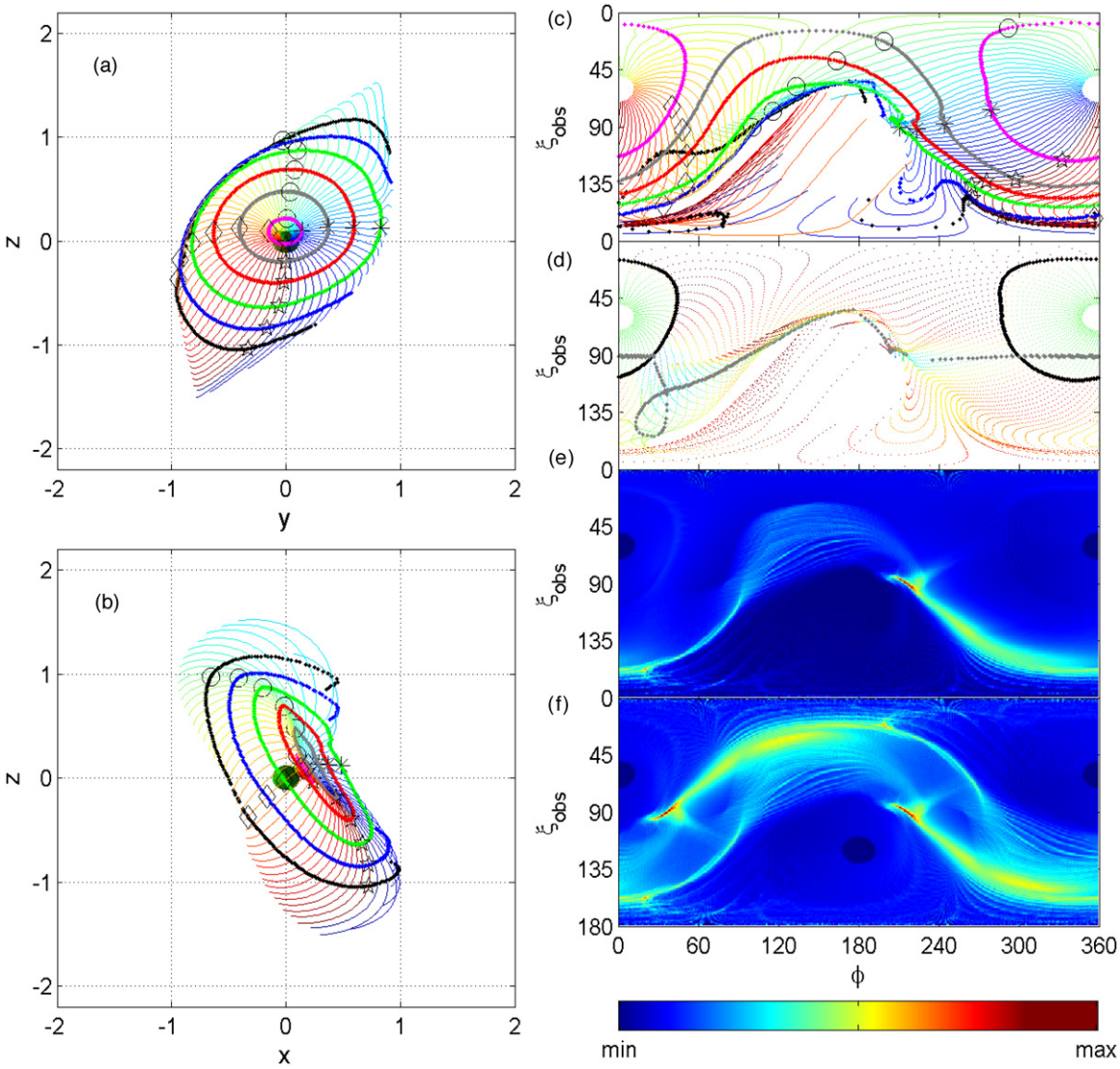

Figure 6. Sky map and field line structure from the TPC model using the FF field. The inclination angle is $\alpha = 60^\circ$. All field lines have $r_{ov} = 1.0$ and are traced to the LC. (a) and (b) Field lines from the north pole viewed from two different directions. (c) Projection of field lines from the north pole onto the sky map. Line colors are the same as in panels (a) and (b). Color rings represent points located at the same distance along the magnetic field lines from the center of NS: pink ($0.25R_{LC}$), gray ($0.50R_{LC}$), red ($0.75R_{LC}$), green ($1.0R_{LC}$), blue ($1.25R_{LC}$), and black ($1.50R_{LC}$). Asterisks, circles, diamonds, and stars are added to help in identifying field lines. (d) Line plot of the sky map with each point colored by 4-current length ϱ (see Equation (4)); $\varrho = 0$ corresponds to the middle of the color bar. NCS is indicated by the gray dots, and the black circles correspond to the actual size of the star in the simulation ($R_N^{sim} \sim 0.19R_{LC}$). (e) Sky map from field lines from the north magnetic pole. (f) Sky map from both poles. In panels (e) and (f), zero brightness corresponds to the dark blue as indicated by "min" in the color bar. See the text for more details.

(A color version of this figure is available in the online journal.)

corresponding sky maps are shown in Figure 6 for inclination $\alpha = 60^\circ$. In order to better see the origin of the sky map features, we mark different field lines with different colors in panels (a) and (b), and use the same color convention to plot the sky map in panel (c). To guide the eye, we also plot six color rings crossing the field lines in panels (a) and (b) and their projections onto the sky map in panel (c). Points on each ring are located at a fixed distance, s, from the center of NS, measured *along* the field lines. The six rings span from $s = 0.25R_{LC}$ to $1.50R_{LC}$ with an interval of $0.25R_{LC}$. As the size of the star in the simulation is relatively large, $R_N^{sim} = 0.19R_{LC}$, tracing emission from the surface out would leave large gaps on the sky map surrounding the poles. To fill these gaps, we add tracing of radiation from inside the star, where we impose a vacuum dipole field down to the radius $R_N = 0.01R_{LC}$. This makes the effective size of the star for the purposes of sky map calculation to be R_N. As the FF field is nearly dipolar close to the star, the matching to the vacuum field is easy to achieve. In panel (d), we make the line plot of the sky map as in panel (c), but the lines are colored with the value of 4-current length ϱ, defined in Equation (4). Since current drops rapidly with radius, the actual color scale is set by ϱr^2. Note that in this panel, $\varrho = 0$ corresponds to the middle of the color bar. The black semi-circles around the pole indicate the size of the star in the simulation R_N^{sim}. At smaller radii, where the FF field is not available, ϱ is taken to be zero. Panels (e) and (f) display the brightness of the sky map. Note that panel (e) shows the sky map brightness from the north pole only, as in all previous panels, while panel (f) is a complete sky map containing both poles. In calculating the sky map brightness, the synchrotron pitch angle θ_p is taken to be zero.

First of all, the pattern of the sky map from the FF field, as seen in Figure 6, is very different from the sky map from the TPC model using the vacuum magnetic field (Dyks & Rudak 2003; Dyks et al. 2004; see also Figure 12 below). As noted in

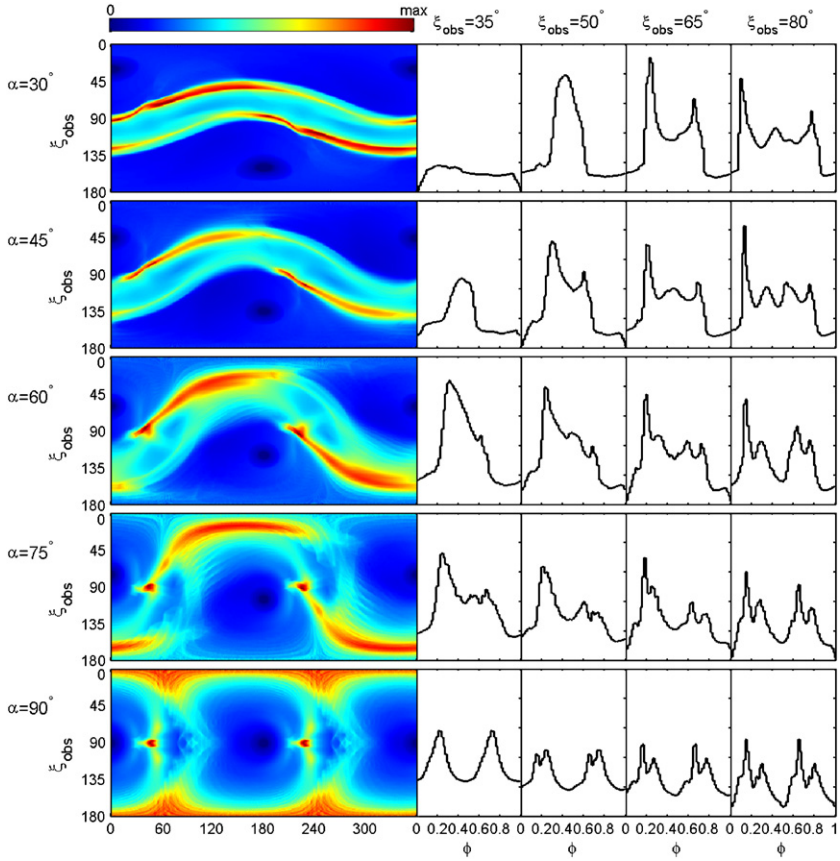

Figure 7. Light curves (right) predicted from the TPC model using the FF field at various magnetic inclination angles α and observer viewing angles $\zeta_{\rm obs}$. The corresponding sky maps are shown on the left. Emission zone is centered on LOFLs, extending to LC. A synchrotron pitch angle $\sin\theta_p = 0.1$ is applied. The curves at the same α have the same normalization.

(A color version of this figure is available in the online journal.)

BS10, the aberration formula used in earlier works needs to be corrected, and this reduces the strength and increases the width of the caustics. The FF sky map here is also very different from the corrected vacuum sky map (see Figures 4(b) and 4(d) of BS10, or Figure 12 below). The main differences include (1) there is no caustic or local enhancement produced near the NS; (2) all caustics are formed near the LC.

It is important to understand why the FF field gives such a dramatically different appearance of the sky map even though the structure of the FF field is similar to that of the vacuum field close to the star. We find that this effect can be attributed to the shape of the polar cap. Recall that in Figure 4, the FF polar cap is more circular than its vacuum counterpart. More importantly, the FF polar cap is larger. The caustics in the vacuum field are significant in the open field line region, but weaken toward the LOFLs, tending to disappear if the emission is calculated from the field lines further in the closed zone. As the larger FF polar cap encloses the vacuum polar cap, the LOFLs of FF would map into the closed field zone of the vacuum magnetosphere. This explains the lack of caustics close to the NS surface using the FF field.

Next we discuss the structure of the FF sky map for the TPC model (Figure 6). Each pole contributes to two main caustic structures. For the field lines coming from the north pole (Figures 6(c)–6(e)), the location of the caustics roughly coincides with the green ring, and in the sky map it appears as a broad arc (Figure 6(e)). At early phases ($\phi < 120^\circ$), the caustic is mainly caused by the sweepback of field lines on the sky map (yellow field lines in Figures 6(a)–6(c)). This caustic is relatively weak and narrow. At later phases, there is a bright "knot" where emissions from neighboring field lines cross each other on the sky map (near the intersection of light blue field lines and the red or green rings in Figure 6(c)). This knot and the adjacent region contribute to the most of the second caustic, which is brighter and wider. The knot can also be seen in panel (a), where light blue field lines fall close to each other. There is large shear between neighboring field lines corresponding to large current flow. The field lines resulting in the knot enter the current sheet, and this feature persists in many different simulations.[6]

Adding the emission from both poles, there can be up to four peaks in the gamma-ray light curve. A large fraction of the area of the sky map includes contributions from both poles. Besides the two bright caustics, emission from other regions is mostly smooth, except in regions close to the LC (e.g., the tips of red and cyan lines in panel (a)). Comparing with Figure 5, we find that these regions are deeply embedded in the strong current layer, where the field structure may not be well resolved in the simulation.

Figure 7 shows a gallery of representative light curves predicted from the TPC model in the FF field for different

[6] We note that Contopoulos & Kalapotharakos (2010) observed similar features as they evolve the system for longer time. We have also checked simulations with still higher resolution, and with finite conductivity using the prescription by Gruzinov (2007b), and find that the "knot" appears in all simulations.

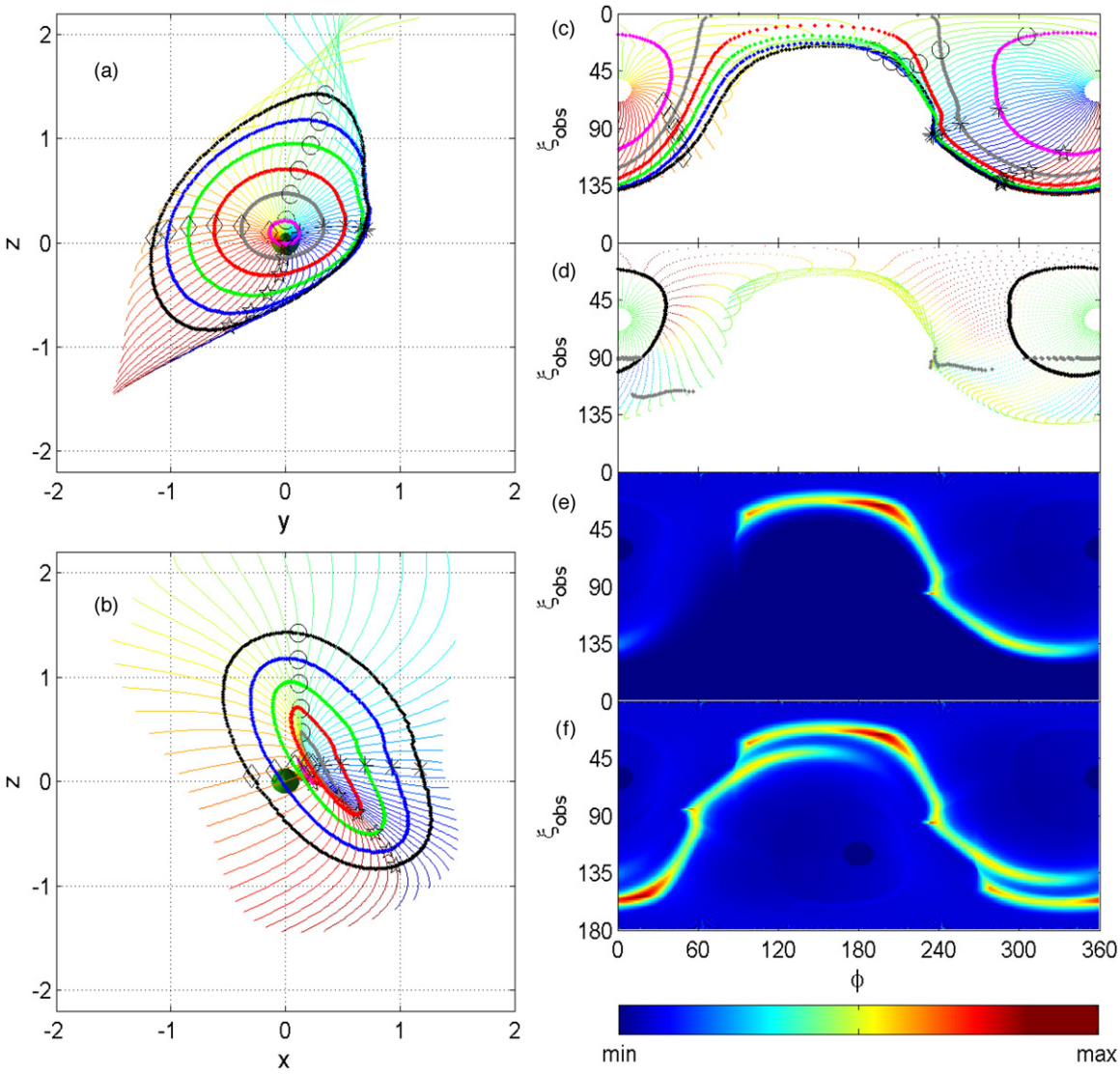

Figure 8. Same as Figure 6, but for the SL model, with an inclination angle $\alpha = 60^\circ$. Field lines all have $r_{\rm ov} = 0.9$ and are traced to the cylindrical radius $R = 1.2R_{\rm LC}$. (A color version of this figure is available in the online journal.)

inclination angles and observer viewing angles. In this plot we have chosen $\sin\theta_p = 0.1$ to show the effect of non-zero pitch angle. We see that this smoothes the sky map substantially, as can be seen by comparing the $\alpha = 60^\circ$ sky map in this figure with Figure 6. Nevertheless, the light curves generally exhibit irregular shapes with up to four peaks. The central part of the light curves is typically brighter because both poles contribute. The caustic structure due to field line sweepback is smoothed and mixed with the overlapping region from another pole, while the caustic from the vicinity of the "knot" is still prominent. Also note that some of the troughs in the light curves are due to the finite size of the poles.

Comparing the light curves of Figure 7 with observations, one generally fails to obtain a clean double-peak profile. At larger inclination angles, the trend is to have two very broad humps instead of narrow peaks. We have tried to restrict the geometry of the emission zone by tuning the parameters $r_{\rm max}$ and $R_{\rm max}$, and found that they do not improve this situation. Moreover, we have also considered simulations with higher resolution and different diffusivity; the appearance of the sky map and the bulk behavior of the light curves does not change qualitatively between different runs.

5. THE SEPARATRIX LAYER MODEL

The difficulties in obtaining double-peaked light curves from LOFLs with the TPC model in the FF field caused us to consider different locations for the emission region. In this section, we study the emission from a set of field lines in the open volume that are still close to the LOFLs. This is motivated by the distributed nature of the return current in oblique rotators. We will refer to this model as the separatrix layer (SL), as the emission region is concentrated in a layer in the vicinity of the separatrix. In practice, we choose $r_{\rm ov} = 0.9 - 0.95$ for the SL model. In Figure 8, we plot the field lines and the corresponding sky maps with $r_{\rm ov} = 0.9$, for inclination $\alpha = 60^\circ$. The emission zone extends from the NS surface to cylindrical cutoff radius $R_{\rm max} = 1.2R_{\rm LC}$. We organize the six panels in the same way as in Figure 6.

The SL model produces two bright and narrow caustics on the sky map. Comparing the TPC sky map with that of the SL model (i.e., moving from $r_{\rm ov} = 1.0$ to $r_{\rm ov} = 0.9$), we see that the weak caustic due to field line sweepback on the left of Figure 6(c) no longer exists, while the caustic associated with the "knot" has evolved to a strong caustic spanning a large

portion of the observer's viewing angle. The "knot" is no longer present. Combining the contribution from the two poles gives rise to two caustics in panel (f).

The origin of the caustics can be traced from panels (a) to (c): we clearly see that the red, green, blue, and black rings overlap at the locations of strong caustics. Therefore, the formation of the caustics is not due to the coincidence that emission from *different* field lines congregates on the sky map (as is the case for caustics in the vacuum field form), but the emission from *one* field line arrives simultaneously, piling up on the sky map. We call this effect "sky map stagnation" (SMS). In Figure 8, we see that SMS starts to develop at a distance from the star along field lines of $0.75R_{\rm LC}$ (beyond the red ring). This corresponds to the outer magnetosphere. The SMS phenomenon covers about one half (π radians) of magnetic azimuth on each pole. Therefore, the full caustic structure caused by SMS sweeps a large fraction of the sky map, giving rise to two sharp peaks in the resultant light curve.

In Appendix D, we show that SMS is a natural consequence of the rotating split monopole solution of Michel (1973b). The direction of particle motion in this field is exactly radially outward, and the winding of the field lines into spirals compensates for the time delay effect. The FF field of the aligned rotator (Contopoulos et al. 1999) approaches the split monopole solution beyond the LC. The oblique rotator also asymptotes to the inclined split monopole solution (Bogovalov 1999, S06), and this causes the caustics in a general FF field. To check this, we have examined the field geometry of open field lines near and beyond LC. We find that the field resembles well the split monopole field. The deviations, which are stronger for lines with larger $r_{\rm ov}$, prevent SMS from occurring on all open field lines. We note that the split monopole field is just one out of many field line configurations that can result in SMS (see Appendix D).

We also constructed sky maps from different open volume coordinates, ranging from $r_{\rm ov} = 0.95$ to $r_{\rm ov} = 0.60$. We find that for smaller values of $r_{\rm ov}$ the SMS behavior is stronger. At $r_{\rm ov} = 0.60$, SMS is achieved for all field lines. This suggests that as we shift toward the center of the open flux tube, the split monopole solution provides a better approximation of the field geometry (see also Figure 10). We also examined the sky map from other inclination angles ranging from $\alpha = 15^\circ$ to 90° (see also Figure 9 below). We find that SMS is in fact a general feature of the FF field.

One consequence of SMS is that the intensity of the caustics is proportional to the length of particle trajectories within the emission zone, if emissivity is constant along the trajectory. We have chosen to cut off the radiation at $R_{\rm max} = 1.2R_{\rm LC}$, which is arbitrary. Choosing a larger cutoff radius will result in brighter and sharper peaks, and vice versa. As emphasized in Section 3, we have used the assumption of constant emissivity along particle trajectories rather than field lines. The two different treatments do not produce significant differences at radii of order of $R_{\rm LC}$ (our approach gives slightly fainter peaks); nevertheless, this approach is more self-consistent and sets the framework for future work (e.g., spectral calculations).

Another consequence of SMS is that the curvature radius $R_{\rm cur}$ of the particle trajectories becomes much larger than the curvature radius of magnetic field lines. One extreme example is the curvature radius of the trajectory in the split monopolar field, which equals infinity, even though the field lines are curved. We have calculated $R_{\rm cur}$ along the open field lines of the FF field (see Appendix C for methodology), and found that $R_{\rm cur}$ generally increases as particles travel farther along the field line, and can reach about $10R_{\rm LC}$ at the LC. Such large curvature radius makes curvature radiation potentially inefficient, and a non-zero pitch angle helps with radiation efficiency, which justifies our inclusion of this effect.

We comment on the IAG model by Qiao et al. (2004, 2007). The choice of $r_{\rm ov} = 0.90$ is consistent with the IAG region. However, the emission of the IAG model is thought to originate relatively close to the NS surface, up to the NCS. As seen from Figure 6, no caustic can form in the inner region of the magnetosphere since the field line is still far from approaching the asymptotic split monopole regime. The IAG model also suffers from the more serious problem that only a small fraction of field lines cross the NCS (see Section 6).[7]

Figure 9 collects the light curves of the SL model for five different inclination angles and four observer viewing angles. The emission is centered on $r_{\rm ov} = 0.9$ (for $\alpha = 30^\circ$ and 45°) and at $r_{\rm ov} = 0.95$ (for $\alpha = 60^\circ$, 75°, and 90°). The emission is prescribed up to cylindrical radius $R_{\rm max} = 1.5R_{\rm LC}$. Due to SMS, the intensity of the calculated light curves depends on how far the emission is traced. To examine the relative importance of emission contributed from different regions, we also plot the light curves originating from within cylindrical radius $R_{\rm max} = 0.9R_{\rm LC}$, indicated as gray lines. There are several features worth noting as we discuss below.

First, we see that the double peak structure is a common feature for most of the light curves. Similar to the conventional TPC and OG models using the vacuum field (Watters et al. 2009), the double peak feature is most likely to appear at relatively large α and $\zeta_{\rm obs}$. Second, we see that emission outside the LC dominates the peak brightness, while the bridge emission is from inside the LC. This is expected from SMS. As a consequence, the intensity contrast at peak and bridge reflects how far the SL extends beyond the LC. For many viewing angles, the first peak tends to be stronger than the second peak. This is due to our assumption of constant emissivity and simplified choice of emission zone boundaries. More physics has to be included to accurately constrain the peak intensities. Finally, without smoothing due to the non-zero pitch angle, the SMS tends to produce reflection-asymmetric light curves. That is, both peaks have a sharp rise and a relatively smooth decay. This appears to be inconsistent with some of the observed gamma-ray pulsar light curves (e.g., light curve of the Vela pulsar (Abdo et al. 2009b), which has a "horn" structure, symmetric upon reflection around the middle of the bridge). By adding a small pitch angle, the FF light curves are smoothed and become more reflection symmetric (e.g., the light curve with $\alpha = 60^\circ$ and $\xi_{\rm obs} = 50^\circ$).

It remains to explain why we choose $r_{\rm ov}$ between 0.90 and 0.95, justifying the emission zone as being in the SL. In Figure 10, we show a series of sky maps with inclination $\alpha = 75^\circ$ from $r_{\rm ov} = 0.80$ to $r_{\rm ov} = 1.0$, using $\sin\theta_p = 0.1$ smoothing. From the top panel, we see that at small $r_{\rm ov}$ SMS develops on all field lines, but only covers a relatively small fraction of the sky map. Emission from two poles does not overlap. Consequently, four peaks appear in typical light curves. As one increases $r_{\rm ov}$, on the one hand, the sky map coverage from each pole increases, reducing the gap region between the two poles; on the other hand, the number of field lines that exhibit SMS decreases, reducing the intensity of two of the four peaks. At around $r_{\rm ov} = 0.90$–0.95, emission from both

[7] The IAG model was further developed recently by Du et al. (2010) where it was called the "annular gap." Their assignment of non-uniform emissivity along field lines may avoid the problem of the lack of caustics.

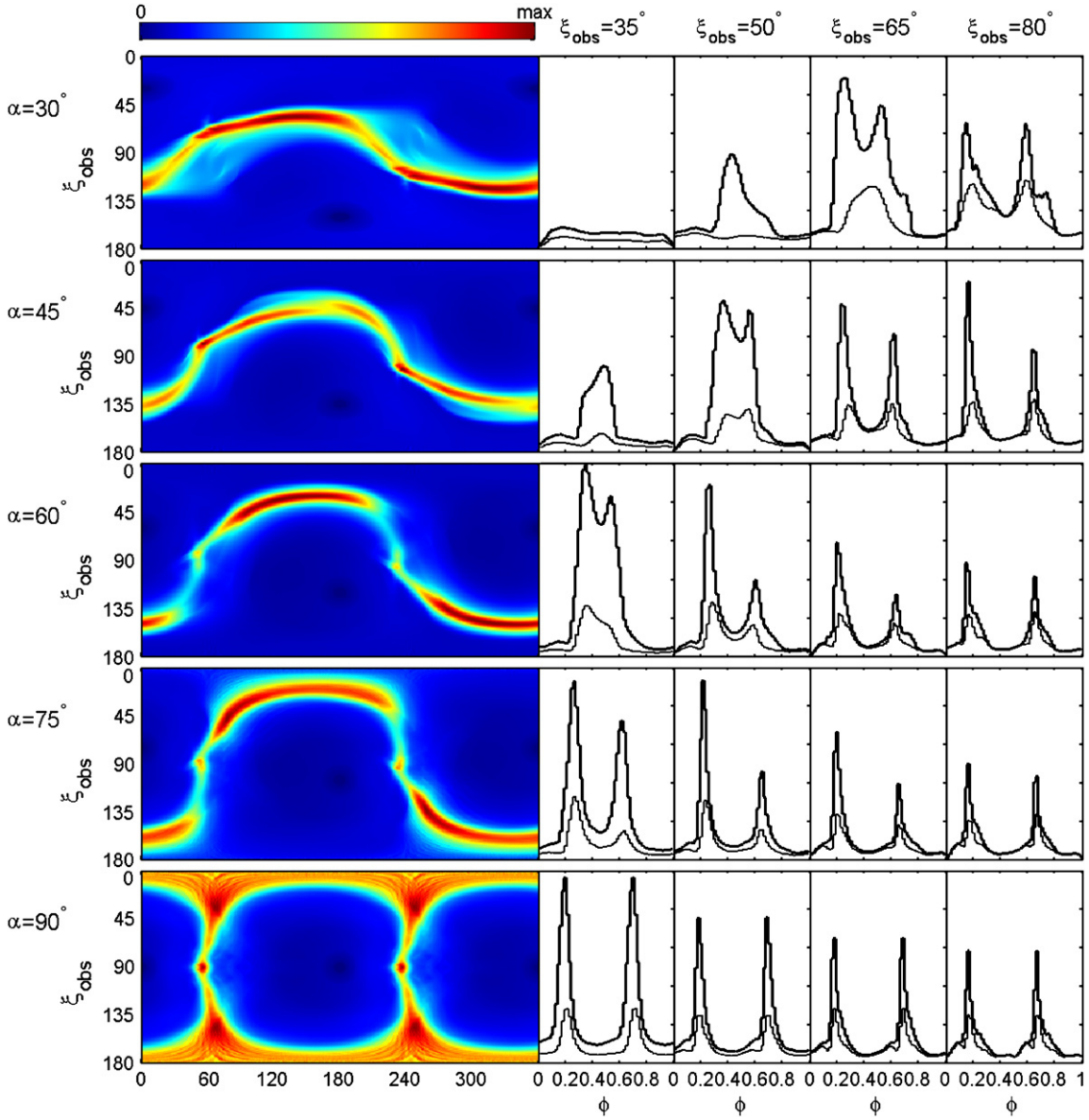

Figure 9. Same as Figure 7, but for the SL model. For inclination angles 30° and 45°, we have chosen $r_{ov} = 0.9$, and the rest use $r_{ov} = 0.95$. For all angles, $\sin\theta_p = 0.1$. For the sky maps and the light curves in black, the emission is traced to cylindrical radius $R = 1.5R_{LC}$. Gray curves show the contribution from the inner magnetosphere, $R < 0.9R_{LC}$.

(A color version of this figure is available in the online journal.)

poles starts to overlap on the sky map, and SMS remains strong for a number of field lines. Upon increasing r_{ov} further toward LOFLs, a significant fraction of the sky map is contributed by two poles, SMS weakens, and the prominent "knot" appears. A similar trend is observed for simulations with other inclination angles.

In sum, we have shown that the SL model with r_{ov} between 0.90 and 0.95 is capable of producing double peak light curves in a wide range of geometric parameters. We will discuss the origin of SL emission in Section 7. The fact that the emission zone responsible for the caustics in the SL scenario is located in the outer magnetosphere is reminiscent of the OG model. However, there are two key differences between the SL model and the conventional OG. First, the OG model is based on the charge-separated magnetosphere, where the formation of the gap is thought to occur only on field lines that cross the NCS. On the other hand, the SL model assumes that the emission zone extends all the way from the stellar surface to beyond the LC on all field lines at a given open volume flux surface, regardless of whether these lines cross the NCS. Second, at a fixed line of sight, most emission, especially the two peaks, are contributed by one pole in the conventional OG model. In contrast, in the above SL model, both poles contribute to the observed emission, particularly, with each pole contributing one peak. This is similar to the TPC model.

6. THE OUTER-GAP MODEL

In this section, we discuss the sky maps and light curves from the OG model using the FF field. A key ingredient of the OG model is the NCS, which determines both the radiating field lines and the extent of emission on these field lines. In the case of the vacuum dipole field, NCS is simply the surface where $B_z = 0$. As a result, emission from the north pole mostly contributes to the $90° < \zeta_{obs} < 180°$ portion of the sky map, and the south pole mainly contributes to the other half. In the FF magnetosphere,

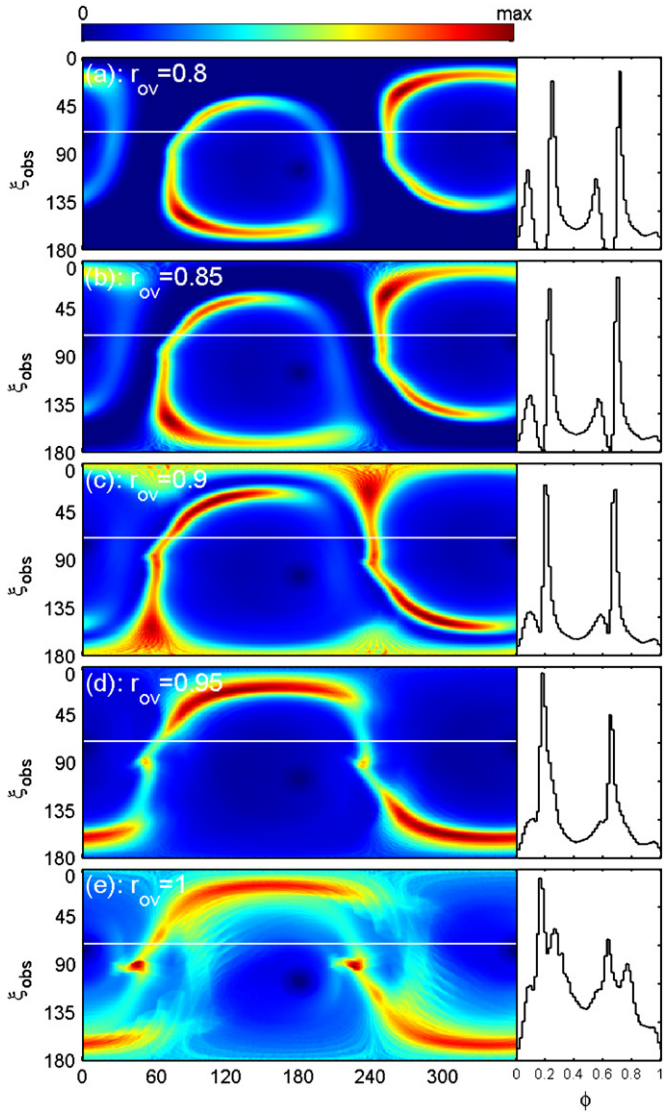

Figure 10. Comparison of sky maps with different r_{ov}. The inclination angle is $\alpha = 75°$. Field lines are traced to $R = 1.2R_{LC}$ except for $r_{ov} = 1.0$ which is traced to $R = 1.0R_{LC}$. $\sin\theta_p = 0.1$ is used for all plots. On the right are the light curves with $\xi_{obs} = 70°$.

(A color version of this figure is available in the online journal.)

we can determine the NCS by finding where $4\pi\rho = \nabla \cdot \boldsymbol{E} = 0$. Guided by the recent work that proposed shifting the inner boundary of the OG toward the star (e.g., Hirotani 2007), we allow emission from the full length of each field line that crosses the NCS. This does not result in extraneous peaks as can happen in the vacuum field, but just maximizes the sky map coverage of the OG model, improving the bridge emission.

In Figure 11, we show the sky map of the OG model for the FF field with $r_{ov} = 0.90$. Because the SL model includes emission from *all* field lines with this r_{ov}, the sky map of the OG model is simply a subset of that of the SL model. In fact, Figure 11 is just part of Figure 9, except the value of r_{ov} there is slightly different (0.9 versus 0.95). Assigning emission only to NCS-crossing field lines almost always eliminates one peak from the light curve. The remaining peak is from the SMS effect of the south pole. The north pole contributes very little to the light curves.

The reason for the elimination of one peak in the OG model is best seen in Figure 8 of the previous section. In panel (d), the location of the NCS on the sky map from the north pole is indicated by gray dots. We can see that only a fraction of field lines cross the NCS. These field lines span roughly 180° in magnetic azimuth on the polar cap. This is to be compared with the case of the vacuum field, as in Figure 12, where for similar geometry, almost all field lines cross the $\boldsymbol{\Omega} \cdot \boldsymbol{B} = 0$ surface (presumably the NCS) eventually. For the same r_{ov}, the FF field lines are "straighter" than their vacuum counterparts, and a large fraction of them do not turn horizontal inside the LC (e.g., compare lines marked with circles in Figures 8 and 12). Therefore, using the FF field, half of the field lines end up being non-emitting under the framework of the OG model.[8] Consequently, half of the bright caustics in panel (e) of Figure 8 are missing. Combining the two poles, there is only one bright peak left. This is a dramatic difference from the results using the vacuum field.

In Figure 11, we confirm that for all inclination angles, most of the light curves have only one prominent peak. In many of these light curves, the shape of the peak as well as the bridge emission is very similar to those produced by the OG model using the vacuum field, but the second peak is missing, or degrades into a weak hump. The weak hump is produced from the same pole as the main caustic, and mostly due to the continuation of the main caustic (e.g., the panel with $\alpha = 60°$, $\xi_{obs} = 50°$). Given the weakness of the hump, it is unlikely to play an important role when more physics is added to relax the assumption of constant emissivity.

In addition, we have experimented with the effect of inward emission. This effect was used in the original version of the OG model (Cheng et al. 1986a, 1986b), and re-considered in Takata et al. (2008). We find that the inward emission itself will produce two peaks whose shapes are similar to the conventional OG model using the vacuum field. Both peaks are relatively weak, and the bridge emission is almost half the brightness of the peaks. More problematically, the first peak lags the radio peak by more than 180°. Adding to this the main peak from the outward emission, there can be three peaks in total. Therefore, inward emission appears unlikely to play an important role.

7. DISCUSSION

We have shown that using the FF field, conventional TPC and OG models no longer work as well as they do in calculations using the vacuum dipole field. Alternatively, we find that the SL model, where emission comes from open field lines that lie just in the vicinity of the separatrix (including the strong current layer inside the LC and the current sheet outside the LC), is very promising in reproducing the prevailing double peak features of gamma-ray pulsar light curves. This model works due to the SMS effect, which is unique to the FF field and occurs as the field becomes increasingly split-monopolar with radius. Our calculations of the SL model in Section 5 work mainly on the geometric grounds with little physical input. In

[8] Note that the charge density inside the artificially large stellar radius of the FF simulation (R_N^{sim}) in Figure 8 is simply taken from the first term on the right-hand side of Equation (3); therefore, the gray dots inside the black circle are roughly a straight line at $\xi_{obs} = 90°$ (corresponding to $B_z = 0$). Outside the black circle, the gray dots are generally below $\xi_{obs} = 90°$, indicating that the location of the NCS in the FF field is further out than determined from the classical $\boldsymbol{\Omega} \cdot \boldsymbol{B} = 0$ criterion. The difference is more significant in regions marked with diamonds than regions marked with asterisks. Although there is a jump in the location of the NCS on the left of panel (d) in Figure 8 due to the large size of the star in the simulation, it is also clear from the plot that it does not affect our selection of NCS-crossing field lines.

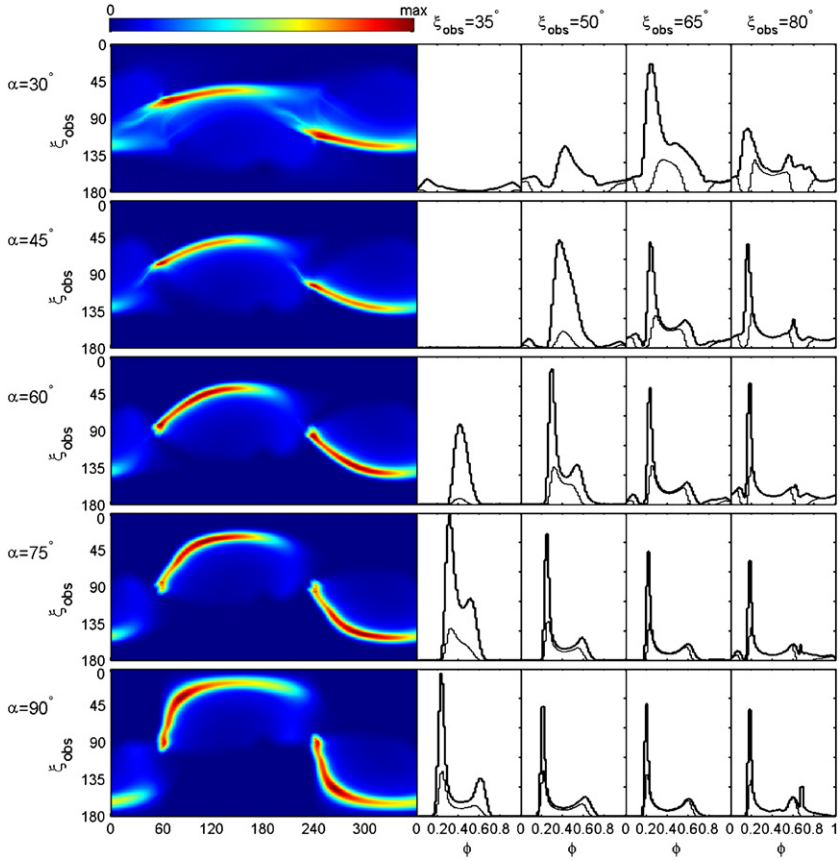

Figure 11. Same as Figure 9, but for the OG model, and emission zone is centered on $r_{ov} = 0.90$.
(A color version of this figure is available in the online journal.)

this section, we discuss the implications of these results to pulsar gamma-ray radiation mechanism and compare our results with observational data.

7.1. Applicability of the FF Field

The FF field provides a more realistic model for the pulsar magnetosphere than the vacuum field because it takes into account the field distortions due to self-consistent currents caused by pulsar spindown. The basic assumption of the FF approximation is that pair creation is so efficient that it fills the magnetosphere with abundant pair plasma to make it a perfect conductor everywhere. Real pulsar magnetospheres are more complicated due to dissipation and reconnection in the current sheet, formation of gaps, and the presence of differential rotation (Timokhin 2007a, 2007b).

One way of testing the robustness of the result obtained in this paper is to consider fields from strong-field electrodynamics (SFE) introduced by Gruzinov (2007a, 2008a, 2008b), which generalizes the FF equations to include dissipation. In SFE, the FF condition $\boldsymbol{E} \cdot \boldsymbol{B} = 0$ is relaxed in space-like regions, where the Ohmic dissipation is present, while time-like regions are still non-dissipative. The dissipation and reconnection in the FF current sheet may be better modeled with SFE. In addition, vacuum gaps in the pulsar magnetosphere may also be considered as dissipative regions, where $\boldsymbol{E} \cdot \boldsymbol{B} \neq 0$. We have implemented SFE formulation into our FF code by replacing the FF current by the SFE current (see Equation (6) of Gruzinov (2007b)). The conductivity scalar $\sigma = \sigma(E_0, B_0)$ is taken to be constant. The natural scale of σ is Ω/c^2, which we denote by $\sigma = 1$. We have run our simulation with different values of σ around 1. We find that the overall field configuration is more smooth than the FF field configuration. Particularly, the "knot" in the sky map from LOFLs which penetrate the current sheet becomes less prominent. The strong current layer inside the LC is not changed qualitatively, but the current sheet outside the LC is smoothed appreciably. More energy is dissipated in the magnetosphere, and the total Poynting flux decreases by about 10% over about $1R_{LC}$.

Despite the fact that SFE produces smoother magnetospheric structure, we find that the resulting sky maps and light curves do not differ qualitatively from the results with the FF field presented in this paper. Therefore, we believe that our result is robust and may also be applicable to dissipative magnetospheres with moderate levels of dissipation.

7.2. The Origin of the Separatrix Layer Emission

We have shown that if pulsar high-energy emission originates from open field line regions in the vicinity of the separatrix, extending from the NS surface to beyond the LC, two bright caustics will form due to SMS. Currently, there is no theory directly pointing to the existence of the SL emission; however, based on the geometric location of the SL, there are clues about its origin.

1. Modified SG/TPC model. We note that SMS is already significant at $r_{ov} = 0.95$, which is very close to LOFLs. Also, in our calculation, the emission zone is assumed to have a Gaussian profile with width $\Delta r_{ov} = 0.025$ centered on r_{ov}. Therefore, the edge of the emission zone can be considered on the LOFLs. This emission zone geometry is

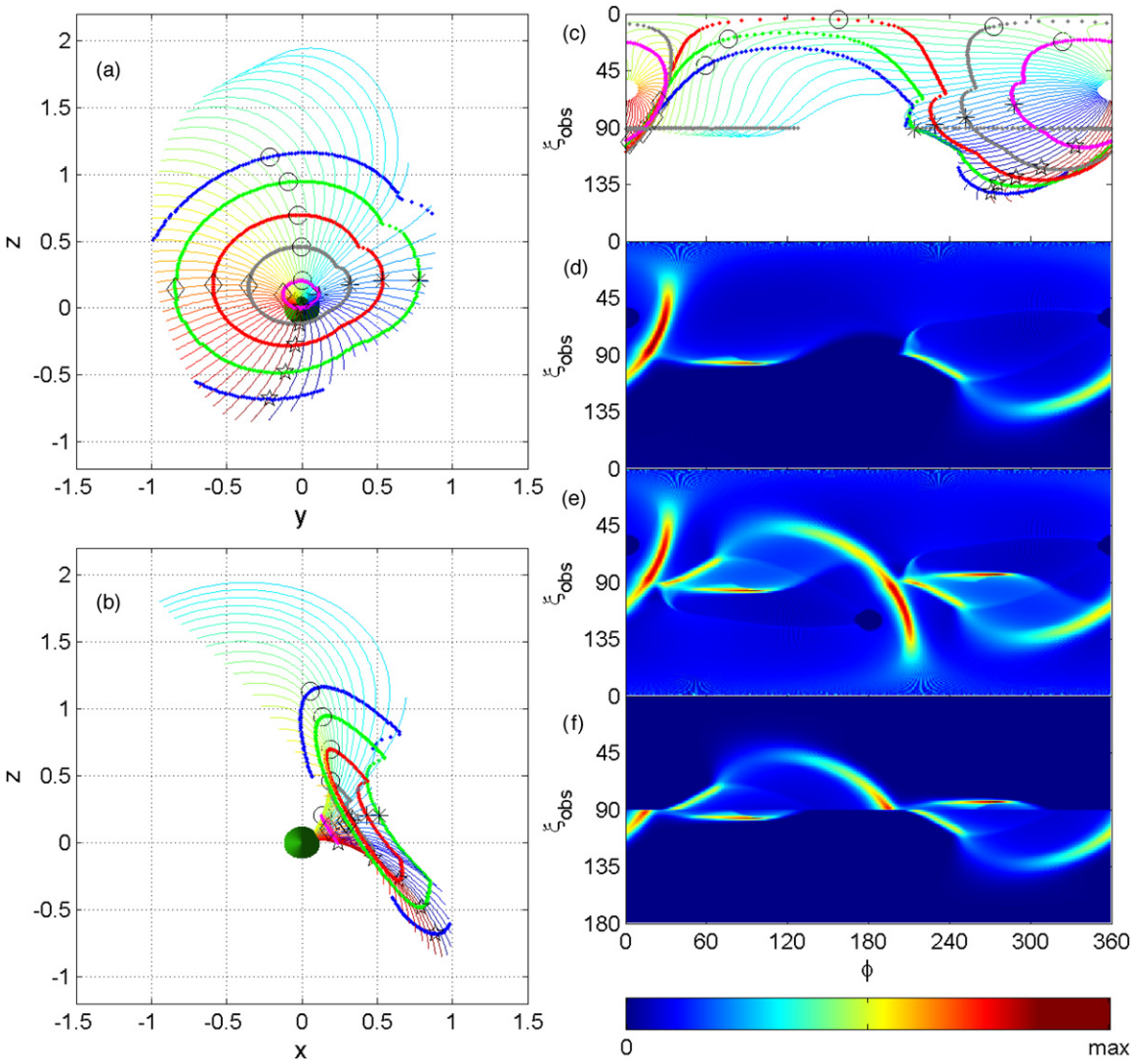

Figure 12. Sky map and field line structure using the vacuum field presented for comparison with the SL model of the FF field from Figure 9. The inclination angle is $\alpha = 60^\circ$. Field lines all have $r_{ov} = 0.9$ and are traced to the LC (cylindrical radius $< R_{LC}$). (a) and (b) Field lines from the north pole viewed from two different directions. (c) Line plot of the sky map based on field lines from the north pole. Line colors are same as in panels (a) and (b). Color rings represent points located at the same distance along the magnetic field lines from the center of NS: pink ($0.25R_{LC}$), gray ($0.50R_{LC}$), red ($0.75R_{LC}$), green ($1.0R_{LC}$), blue ($1.25R_{LC}$), and black ($1.50R_{LC}$). Asterisks, circles, diamonds, and stars are added to help in identifying field lines. Gray diamonds at $\zeta_{obs} \sim 90^\circ$ show the location of the NCS on these field lines. (d) Sky map from the north pole that results from (c) after including emission on every field line at $r_{ov} = 0.9$. The emission is included from the star to the cutoff radius. (e) Sky map that results when the emission from both poles is superimposed. This map incorporates emission regions of both TPC and OG models (formally, the TPC model is usually centered on $r_{ov} = 1$, but the picture is similar at $r_{ov} = 0.9$). While it generally results in too many peaks, this plot demonstrates the origin of all caustics in the vacuum field. The clustering of rings in panel (c) indicates enhanced caustic emission in the sky map, although here the caustics are caused by near overlap of neighboring field lines, rather than SMS from each field line. (f) Sky map that results from panel (e) when emission below NCS is removed. This is the classical OG model.

(A color version of this figure is available in the online journal.)

consistent with the SG model. Therefore, if the thickness of the pair formation front is as large as $\Delta r_{ov} = 0.025 - 0.05$, a modified SG model may be able to produce the desired two peak light curves. Such SG must extend at least to the LC to produce sharp peaks. Recent SG/TPC models consider emission from smaller r_{ov} flux tubes (e.g., Venter et al. 2009). Given that in the FF field only the field lines with $r_{ov} < 0.95$ are truly open and do not close through the current sheet, it is likely that at least geometrically the SL model can be considered as an extension of TPC and invokes the same field lines. The physical reason for the acceleration on these lines is unlikely to be a SG, however, and is more related to reconnection in the current sheet, as discussed below.

2. Modified OG model. Another clue comes from the distribution of space-like regions in the magnetosphere. Regions of space-like 4-current, which are likely to develop instabilities and could have accelerating fields (Gruzinov 2007b), are preferentially located beyond the NCS. Similar locations are typically invoked in OG models, although for reasons that rely on complete charge separation in the magnetosphere. Even if the OG-type model can be justified based on the sign of 4-current, it would not be sufficient to produce two peaks—the emission has to come from more field lines than those crossing the NCS. Interestingly, looking at Figure 8(d), the regions showing the pile-up due to SMS have values of ϱ near zero, or negative. If small positive values of ϱ can also cause

acceleration, this could explain the emission from the whole flux tube.

3. Association with the strong current. The presence of a strong current layer within the LC and a current sheet beyond LC are general features of the FF field. Strong dissipation and reconnection is expected in such regions (Gruzinov 2007a; Lyubarsky 2008), and the energy release can reach a few percent of the spindown power, probably radiated in X-rays and gamma rays (Lyubarskii 1996). Using Bogovalov's (1999) current sheet solution for the inclined split-monopole, Kirk et al. (2002) were able to reproduce the typical double-peak light curves, indicating that the field configuration around the current sheet beyond the LC is also geometrically favored. Based on the same model, Pétri & Kirk (2005) and Pétri (2009) further reasonably well reproduced the optical polarization of the Crab pulsar and phase-resolved spectrum for the Geminga pulsar. Our result that the SL emission zone resides in the vicinity of the strong current layer and/or current sheet (see Figure 5) implies a connection with the strong current. At higher inclinations, the return current becomes increasingly distributed over the open flux, and it is possible that some of the acceleration takes place on the open field lines. Also, the caustics of emission form in the outer magnetosphere, and the acceleration on these field lines can be affected by the proximity of the *Y*-point. Reconnection near the *Y*-point (or "Y-ring" in 3D) can load the open field lines with plasma and cause field-aligned accelerating fields, akin to auroral double-layers (Arons 2008). Emission from the equatorial current sheet beyond the LC can also be important, as the field lines we invoke for SL trace close to the current sheet in the wind zone. Modeling emission from the current sheet itself is more complicated in FF simulation, since ideal MHD does not apply in the current sheet, and the magnetic field direction abruptly changes in the unresolved current sheet, which leads to tracing errors. This will be studied more in future work. The facts that the bulk of the SL emission is formed at and beyond the LC, and that emission from two poles overlaps on the sky map and forms two peaks only close to the edge of the open flux tube (for $r_{ov} > 0.9$, Figure 10), suggest that the current sheet beyond the LC is responsible for the large part of gamma-ray emission.

Our discussion on the origin of the SL model is highly speculative. A detailed theory of the electrodynamics of current sheets has to be constructed to test these scenarios and uncover the origin of the SL emission.

7.3. Comparison with Observations

One year after launch, *Fermi*–LAT has greatly expanded the number of detected gamma-ray pulsars either by identifying previously unresolved/unidentified sources (e.g., known radio pulsars, millisecond pulsars (MSPs), EGRET sources, supernova remnants, pulsar wind nebulae; Abdo et al. 2008, 2009a, 2009c, 2009g), or by the blind search of LAT sources (Abdo et al. 2009f). Together with previously known gamma-ray pulsar data, a sample of more than 40 gamma-ray pulsars is now available (Abdo et al. 2010), allowing more systematic comparison between observations and theoretical models.

Under the framework of the SL model with the FF field, the double-peak light curves can be produced over a large range of geometric parameters, as shown in Section 5. As a geometric model, it provides robust prediction on the temporal location of the two peaks regardless of the input physics. The phase lag of the first peak relative to the radio peak (which likely coincides with the location of the polar cap on the sky map) ranges from about $\delta = 0.14$ to larger than $\delta = 0.3$, and the separation between the two peaks ranges from zero (i.e., one peak) to $\delta = 0.5$. Smaller phase lag typically corresponds to larger separation, and vice versa, as seen from the caustic structure of Figure 9. Also, larger inclination angles tend to result in larger peak separation. Statistically, our model predicts that the majority of light curves should have widely separated double peaks, pulsars with smaller peak separation are less common, and pulsars with only one peak are possible but rare. Another consequence of the SL model is that smaller peak separation usually indicates stronger bridge emission between the peaks. The best example of this can be drawn from the light curve with $\alpha = 45^\circ$ and $\xi_{obs} = 50^\circ$ in Figure 9.

Based on the current data sample of gamma-ray pulsars, the majority of them show widely separated double-peak pulse profiles, in good agreement with the SL model. A small fraction shows double peaks with smaller separation (e.g., B1716−44, Pellizzoni et al. 2009a; J0007+7303, J1459−60, J1741−0254, Abdo et al. 2009f), but with relatively strong bridge emission, also in qualitative agreement with our result.[9] A few objects show only one peak (e.g., J0357+32, Abdo et al. 2009f; PSR 0437−4715, PSR 0613−0200 Abdo et al. 2009g; J2229+6114, Pellizzoni et al. 2009b). Such pulse profiles may be obtained when the observer's line of sight tangentially cuts through the caustics on the sky map (examples include $\alpha = 30^\circ$, $\xi_{obs} = 50^\circ$ in Figure 9). The small number of such pulsars agrees with the small chance of such tangential incidence. Noticeably, the fraction of single peak MSPs appears to be higher than for normal gamma-ray pulsars (Abdo et al. 2009g). This may reflect the fact that MSPs tend to have smaller inclination angle which increases the chance of tangential incidence. Given the relatively old age of the MSP population, their smaller inclination angle might be caused by alignment torques (Davis & Goldstein 1970; Goldreich 1970; Melatos 2000).

The distribution of phase lags from the SL model is not directly comparable with the latest data since most new gamma-ray pulsars are radio-quiet. For available radio-loud pulsars, we find some agreement, but not always. For example, the phase separation between peaks in B1706−44 appears to be too small to fit our model, as both peaks come in the first half of the rotation. There may be an additional phase lag from the radio peak due to high altitude radio emission from energetic pulsars (Weltevrede & Johnston 2008). Therefore, it is uncertain whether observed phase lag can be used as a reliable diagnostics.

8. SUMMARY AND CONCLUSION

This paper is concerned with high-energy emission from gamma-ray pulsars modeled by the FF field. The FF field takes into account the effect of conducting plasma, and the charges and currents are solved self-consistently using time-dependent simulations. By construction, the FF magnetosphere does not emit because $\boldsymbol{E} \cdot \boldsymbol{B} = 0$ everywhere, but it provides a more realistic approximation to the field structure. The FF field differs substantially from the vacuum dipole field in several ways. First, there is a larger magnetic flux on the open field lines. As a result, the polar cap is larger than the vacuum polar cap. Second, beyond the LC, the FF field has a strong

[9] Note that in Figure 2 of Abdo et al. (2009f), the first peak is placed at phase of 0.3 because most of the new gamma-ray pulsars are radio quiet.

current sheet and field lines approach inclined rotating split-monopole shape. Inside the LC, there is a strong current layer coinciding with the LOFLs. This layer is a thin current sheet for the aligned rotator, which connects to the current sheet outside the LC. The amount of current carried by the current sheet inside the LC decreases with the inclination angle. The inner current sheet disappears completely for the orthogonal rotator. Current distribution on the polar cap varies with α, with a larger fraction of the current closing through the polar cap at larger inclinations, rather than in a thin boundary layer. Third, the charge distribution in the FF magnetosphere contains significant concentration of charge in the current sheet/strong current layer, and the charge distribution in the current sheet for the aligned rotator is substantially different from that of the oblique rotators. Moreover, the NCS is no longer determined by $\boldsymbol{\Omega} \cdot \boldsymbol{B} = 0$, and a large fraction of open field lines does not cross the NCS at all. Fourth, the 4-current in substantial fraction of the FF magnetosphere is space-like, requiring the presence of charges of both signs, which is inconsistent with completely charge-separated picture.

The differences in the field structure of FF and vacuum fields give rise to substantial differences in the resulting theoretical light curves. The polar cap in the FF magnetosphere is more circular and larger than the vacuum polar cap. Therefore, close to the star, the location of LOFLs of the FF field corresponds to closed field line regions in the vacuum field. Due to this effect, the caustics seen in the TPC model using the vacuum field no longer exist in the FF field. Instead, the pattern on the sky map is more complicated: up to four peaks (caustics) may exist, and a large fraction of the sky map is covered by emission from both poles. In addition, there is a bright "knot" region on the sky map associated with the strong current. In any case, we find it difficult to reproduce the typical double-peak profile in the resulting light curves using the TPC model.

We have shown that if we relax the emission zone in the TPC model into a SL, where the emission comes from the open field line regions near the strong current layer/current sheet and extends from the NS surface up to and beyond the LC, two bright caustics will appear. The cause of the caustics is completely different from that in the case of a vacuum field. For a large fraction of open field lines in the outer magnetosphere, the emission from different heights along the field line piles up at the same spot on the sky map, which strongly enhances the sky map brightness at that location. This effect, which we call SMS, is due to the fact that the FF field asymptotically approaches the split monopole field at large radii. As a result, the intensity of the caustics due to SMS effect is determined by the extent of the emission zone. The typical feature of the light curves from this SL model is two sharp peaks with more or less uniform off-peak emission. Each pole contributes to one peak. The rise of the peak is usually sharp while the drop is more smooth. Adding the effect of the non-zero pitch angle smoothes the sky map. This model provides robust prediction on the location and the separation of the two peaks, and the resulting light curves match the general features of most observed gamma-ray pulsar light curves. Although there is no theory predicting the existence of this SL emission, its location in the pulsar magnetosphere strongly suggests its association with the strong current layer and/or current sheet, particularly the current sheet beyond the LC.

The sky map from the OG model can be considered as part of the SL model, restricted only to field lines that cross the NCS. We find, however, almost always that only one peak can form. The reason is that a substantial fraction of the open field lines do not cross the NCS at all. The coverage of the emission on the sky map is similar to that of the vacuum field, but the formation of caustics is due to SMS. Some gamma-ray pulsars recently observed by the *Fermi* telescope show only one prominent peak, and the OG model using the FF field may be relevant to such pulsars. The IAG model also relies on field lines that cross the NCS, and thus suffers the same problem as the OG model. However, because the emission zone in the IAG model is relatively close to the NS, where SMS does not develop, it will be even more difficult to produce any peaks with this model using the FF field.

In constructing models of the emission zones, we assigned emission to flux tubes concentric to the LOFLs. This can be an oversimplification, and the actual emitting flux tube can have a more complicated shape. This is particularly so if reconnection in the *Y*-point region affects neighboring field lines in the outer magnetosphere. The origin of those field lines on the polar cap does not have to be concentric to LOFLs. An avenue that we have yet to explore in detail is to assign emission not per field line, but in the whole volume of the magnetosphere, weighted by some proxy of the magnetospheric dissipation, such as the strength of the current. The gross features of the FF sky maps, such as the caustic formation in the outer magnetosphere due to SMS will likely remain the same; however, the quantitative shape of the light curves may be affected. This will be the subject of future work. In addition, our modeling of pulsar high-energy emission assumes constant emissivity along particle trajectories, which works on a purely geometric basis and serves as the first step in comparing different theoretical models and identifying possible regions of emission. More physics input is needed for a consistent study of pulsar high-energy emission that would reveal the origin of the pulsar magnetospheric accelerator.

We thank Jonathan Arons and Yuri Lyubarsky for helpful discussions. We are also grateful to Ioannis Contopoulos for his constructive suggestions. This work is supported by NASA grants NNX08AW57G and NNX09AT95G. A.S. acknowledges the support of Alfred P. Sloan Foundation fellowship. X.N.B. acknowledges support from NASA Earth and Space Science Fellowship.

APPENDIX A

DERIVATION OF USEFUL RELATIONS IN FORCE-FREE MAGNETOSPHERE

Formal proof of Equations (1) and (2) can be found in Gruzinov (2006). In this Appendix, we summarize Gruzinov's proof and further explain the physical meaning of λ.

Both equations follow from two assumptions: (a) the electromagnetic field is FF and (b) the electromagnetic pattern corotates at angular velocity Ω. Condition (b), when applied to an arbitrary vector field $\boldsymbol{U}$, can be written as

$$[\partial_t + (\boldsymbol{\Omega} \times \boldsymbol{r}) \cdot \nabla]\boldsymbol{U} = \boldsymbol{\Omega} \times \boldsymbol{U}. \tag{A1}$$

For electric and magnetic fields, after some algebra, the above equation can be reduced to

$$\frac{\partial \boldsymbol{E}}{\partial t} = \nabla \times [(\boldsymbol{\Omega} \times \boldsymbol{r}) \times \boldsymbol{E}] + 4\pi\rho(\boldsymbol{\Omega} \times \boldsymbol{r}), \tag{A2}$$

$$\frac{\partial \boldsymbol{B}}{\partial t} = \nabla \times [(\boldsymbol{\Omega} \times \boldsymbol{r}) \times \boldsymbol{B}]. \tag{A3}$$

In line with Gruzinov (2006), Equation (A3), together with the induction equation, implies $\boldsymbol{E} = -\vec{\beta}_0 \times \boldsymbol{B} + \nabla\chi$, where χ is a scalar function to be determined. The fact that the NS is a perfect conductor ensures χ to be constant on the stellar surface, while the FF condition requires χ to be constant along magnetic field lines. Therefore, χ must be constant everywhere, completing the proof for Equation (1).

Gruzinov (2006) proved Equation (2) by using the variational principle. Despite the mathematical beauty of this method, the physical meaning of λ is not explicitly seen. Below we prove Equation (2) from direct calculation.

We begin by substituting Equation (A2) into Ampere's law of Maxwell's equation, and making use of Equation (1), one immediately obtains

$$\nabla \times [\boldsymbol{B} + \vec{\beta}_0 \times (\vec{\beta}_0 \times \boldsymbol{B})] = \boldsymbol{j} - \rho(\boldsymbol{\Omega} \times \boldsymbol{r}). \quad \text{(A4)}$$

It remains to show that $\boldsymbol{B} \parallel (\boldsymbol{j} - \rho(\boldsymbol{\Omega} \times \boldsymbol{r}))$. This becomes obvious since the FF current can be cast into (see Equation (2) of Spitkovsky 2006)

$$\boldsymbol{j} = \rho \frac{\boldsymbol{E} \times \boldsymbol{B}}{B^2} c + \boldsymbol{j}_\parallel, \quad \text{(A5)}$$

where $\boldsymbol{j}_\parallel$ is the current density that is parallel to $\boldsymbol{B}$. Because of Equation (1), the corotation velocity $\boldsymbol{\Omega} \times \boldsymbol{r}$ can be decomposed into the $\boldsymbol{E} \times \boldsymbol{B}$ drift velocity and a component that is parallel to $\boldsymbol{B}$.

In sum, we have reached a remarkably simple and clear formula

$$\lambda \boldsymbol{B} = \boldsymbol{j} - \rho(\boldsymbol{\Omega} \times \boldsymbol{r}) \equiv \boldsymbol{j}^C, \quad \text{(A6)}$$

where $\boldsymbol{j}^C$ is the current density in the CF (Schiff 1939; Grøn 1984). Therefore, in the CF, the magnetic field line and current are parallel to each other. The ratio between j^C and B is denoted by λ and is constant along the magnetic field lines.

APPENDIX B

CURRENT SHEET IN THE FORCE-FREE FIELD

In this Appendix, we show that the current in the current sheet outside the LC in the FF field does not necessarily connect to the star. Our discussion adopts Bogovalov (1999)'s solution. It describes the field structure of a rotating split monopole, and asymptotically approaches to the FF field at large radii. Bogovalov's solution reads

$$\boldsymbol{B}_m = \frac{f_0}{r^2}(\boldsymbol{e}_r - R\boldsymbol{e}_\phi)\eta(r, \theta, \phi), \quad \text{(B1)}$$

where the subscript "m" represents monopole, f_0 is an arbitrary constant, $R = r\sin\theta$ is the cylindrical radius, and

$$\eta(r, \theta, \phi) = D(\sin\alpha \sin\theta \sin(\phi + r/R_{\rm LC}) + \cos\alpha\cos\theta) \equiv D(x), \quad \text{(B2)}$$

where $D(x) = 1$ for $x > 0$ and $D(x) = -1$ for $x < 0$.

The current sheet lies on the surface determined by $x = 0$, namely,

$$\cot\theta = \tan\alpha \sin(\phi + r/R_{\rm LC}). \quad \text{(B3)}$$

Clearly, we have $\pi/2 - \alpha \leqslant \theta \leqslant \pi/2 + \alpha$. One can find the normal direction of this surface to be

$$\boldsymbol{n} = \frac{1}{\sqrt{1 + 2A^2}}(A\boldsymbol{e}_r - \boldsymbol{e}_\theta + A\boldsymbol{e}_\phi), \quad \text{(B4)}$$

where

$$A = [1 + \tan^2\alpha \sin^2(\phi + r/R_{\rm LC})]\tan\alpha\cos(\phi + r/R_{\rm LC}). \quad \text{(B5)}$$

The natural frame to calculate the current in the current sheet is the CF, where the current is given by Equation (A4). In addition to the curl of $\boldsymbol{B}$, the CF current has contribution from the curl of $\vec{\beta}_0 \times \boldsymbol{E}$ term. Therefore, it is useful to define

$$\boldsymbol{H}_m \equiv \boldsymbol{B}_m + \vec{\beta}_0 \times (\vec{\beta}_0 \times \boldsymbol{B}_m) = \frac{f_0}{r^2}[(1 - R^2)\boldsymbol{e}_r - R\boldsymbol{e}_\phi]\eta(r, \theta, \phi). \quad \text{(B6)}$$

The surface current density in the current sheet in the CF is then given by

$$\boldsymbol{J} = \boldsymbol{n} \times (\boldsymbol{H}_m^+ - \boldsymbol{H}_m^-), \quad \text{(B7)}$$

where superscripts "+" and "−" denote the quantities just above and beneath the current sheet.

It is useful to look at two special cases, namely, the aligned and orthogonal rotators. For $\alpha = 0$, we have $\boldsymbol{n} = \boldsymbol{e}_z$. From the above equations, it is obvious that $\boldsymbol{J}$ has both radial and azimuthal components. The radial component connects the current to the star and decreases as $1/r$. The azimuthal component asymptotically approaches a constant. Integrating over a circle with radius r, one obtains the net current carried by the current sheet that connects to the star

$$I_0 = \int_0^{2\pi} J_r\Big|_{\alpha=0} r d\phi = 4\pi f_0. \quad \text{(B8)}$$

Note that I_0 is a constant that does not depend on r, reflecting the conservation of current. One can also check that I_0 equals the amount of current flowing from the star (outside the current sheet), but with a minus sign, as expected:

$$I_{\rm star,0} = \oint_{\theta\neq\pi/2} (\nabla \times \boldsymbol{H})\Big|_{\alpha=0} \cdot \boldsymbol{e}_r r^2 \sin\theta d\theta d\phi = -I_0. \quad \text{(B9)}$$

For $\alpha = 90^\circ$, $A \to \infty$, thus $\boldsymbol{n} = (\boldsymbol{e}_r + \boldsymbol{e}_\phi)/\sqrt{2}$. Plugging into the above equations, one finds that $\boldsymbol{J}$ has only the $\hat{\theta}$ component. This means that the current in the current sheet is not connected to the star, but forms poloidal loops in the $\hat{\theta}$-direction. In the FF field from our simulations, we do observe such loops in the current sheet outside the LC. Since they are not connected to the star, it becomes clear that there is no current sheet in the inner magnetosphere for the orthogonal rotator.

After some algebra, we obtain the general expression of the current carried by the current sheet that is connected to the star

$$\frac{I_{\rm sheet}(\alpha)}{I_0} = \int_0^{2\pi} \frac{\sin\theta}{\sqrt{1 + 2A^2}} \frac{d\phi}{2\pi}, \quad \text{(B10)}$$

where θ is determined by Equation (B3) and A is given by Equation (B5). The quantity does not depend on r, as expected. Moreover, one can check that this quantity also equals the net current flowing from the rest of the star

$$\frac{I_{\rm star}(\alpha)}{I_0} = -\frac{1}{2\pi} \oint \cos\theta \sin\theta D(x) d\theta d\phi, \quad \text{(B11)}$$

where x is given by Equation (B2). The dependence of $I_{\rm sheet}$ on an inclination angle α is shown in Figure 13. We see that the amount of current in the current sheet that is connected to the star monotonically decreases with α. This is related to the degradation of the current sheet inside the LC discussed in Section 2.1.

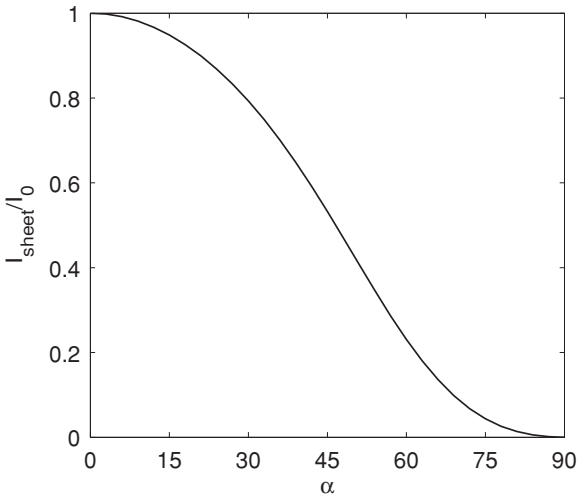

Figure 13. Amount of current in the current sheet of the rotating split monopole that is connected to the star $I_{\rm sheet}$ as a function of the magnetic inclination angle α. $I_{\rm sheet}$ is calculated from Equation (B10), normalized to the value for the aligned rotator I_0, given by Equation (B8).

APPENDIX C

SEGMENT LENGTH AND CURVATURE RADIUS OF PARTICLE TRAJECTORIES

Here, we describe the method for calculating the length and curvature radius of the particle trajectories. For simplicity, we consider particles with zero pitch angle. The discussion here is valid so far as a particle pitch angle is small, as we use in this paper. The direction of particle motion consists of a combination of $\boldsymbol{E}\times\boldsymbol{B}$ drift velocity (or corotation velocity) and velocity parallel to the magnetic field

$$\boldsymbol{e}=\vec{\beta}_d+\alpha\boldsymbol{t}=\vec{\beta}_0+\alpha'\boldsymbol{t}, \tag{C1}$$

where $\boldsymbol{t}\equiv\pm\boldsymbol{B}/B$ is the unit vector parallel to the magnetic field line (without loss of generality, hereafter we assume the radial component of $\boldsymbol{t}$ points outward), and α or α' are obtained by requiring $|\boldsymbol{e}|=1$:

$$\begin{aligned}\alpha&=-\vec{\beta}_d\cdot\boldsymbol{t}\pm\sqrt{(\vec{\beta}_d\cdot\boldsymbol{t})^2+1-\beta_d^2},\\ \alpha'&=-\vec{\beta}_0\cdot\boldsymbol{t}\pm\sqrt{(\vec{\beta}_0\cdot\boldsymbol{t})^2+1-\vec{\beta}_0^2},\end{aligned} \tag{C2}$$

where the plus/minus signs correspond to trajectories along/opposite to magnetic field line. Usually, we expect $\vec{\beta}_0\cdot\boldsymbol{t}<0$ due to field sweepback. Therefore, the outgoing particles always have $\alpha'>0$ and are expected to have $\alpha'>1$ (for reference, the split monopole field has $\alpha'=\sqrt{1+(R/R_{\rm LC})^2}$). For ingoing particles, however, α' is positive inside the LC, negative outside the LC. This means that ingoing particles can return to the star *only* if they are generated inside the LC. Below we consider only the outgoing particles, taking the plus sign in the equations above.

Particle trajectories can be obtained by tracing the direction of motion while rotating the star at the same time. Since $\boldsymbol{e}$ has a corotation component, Equation (C1) ensures that particle trajectories follow the field lines exactly in the CF. Although this is obvious, we still go through the proof, which will be useful for numerical calculations of curvature radius of particle trajectories.

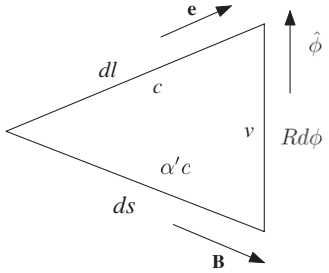

Figure 14. Graphic illustration for particle trajectory calculation.

The proof is best demonstrated in a graphical view. In Equation (C1), the vector equation forms a triangle as shown in Figure 14. The length of each edge is expressed in terms of velocity. Multiplying each of the edges by an amount of time dt, we obtain another interpretation of the graph. The upper edge gives an infinitesimal segment length $dl=cdt$ along the particle trajectory in the direction of $\boldsymbol{e}$. The lower edge becomes $ds=\alpha' cdt$, which marks the corresponding segment length along the magnetic field line. As the particle travels by dl, the star (and the field lines) rotates by an angle $d\phi=\Omega dt=\Omega dl/c=dl/R_{\rm LC}$. Therefore, the entire field line is shifted by $Rd\phi=\beta_0 cdt=Rdl/R_{\rm LC}$ in the azimuthal direction; this corresponds to the right edge. Now we have obtained a closed triangle that is similar to the original velocity triangle. Based on this new interpretation, we conclude that particle trajectory follows the magnetic field line exactly in the CF.

The fact that particle trajectories follow CF magnetic field lines as well as the similarity relations from the velocity and segment triangles provides a natural way to reconstruct particle trajectory. The key relation is between dl and ds, which satisfies

$$dl=ds/\alpha'. \tag{C3}$$

In practice, we originally have a series of segment lengths along field lines $s[i]$. From this formula, one can obtain a series of segment lengths of the corresponding particle trajectory $l[i]$. This further provides the phase of rotation as the particle travels, $\phi[i]$. Finally, the particle trajectory can be reconstructed by rotating each point on the magnetic field line by $\phi[i]$. It is then straightforward to (numerically) calculate the curvature radius of the particle trajectory.

When performing the calculation, however, there can be cases where the square root in Equation (C2) becomes imaginary. This always happens in the vacuum dipole field once the particle travels out of the LC; it also happens occasionally in the current sheet since the ideal MHD does not apply there and one does not expect Equation (C1) to hold. Moreover, across the FF current sheet, the toroidal component of the magnetic field changes sign, resulting in ambiguity in defining "ingoing" and "outgoing" directions. In such regions, the proposed "outgoing" particles may have $\alpha'<1$, which is not desired. Therefore, we modify Equation (C3) into

$$dl=ds/\max(\alpha',1). \tag{C4}$$

In calculating α', if the terms under the square root is negative, we just take them to be zero.

One can further show the analytical expression for the curvature radius of particle trajectory based on the discussions above:

$$\frac{1}{R_c}=\left|\frac{\boldsymbol{\Omega}\times\boldsymbol{e}}{c}+\alpha'\frac{d\boldsymbol{e}}{ds}\right|. \tag{C5}$$

Numerical experiments show that the curvature radius obtained from this approach has very similar accuracy to the first method.

APPENDIX D

CONDITIONS FOR SKY MAP STAGNATION

According to the formulae of aberration (Equation (C1)) and time delay (Equation (6)), the condition for emission along a magnetic field line to become stagnant on the sky map is

$$\boldsymbol{B} \cdot \nabla e_z = 0, \qquad \boldsymbol{B} \cdot \nabla(\phi_e + \boldsymbol{r} \cdot \boldsymbol{e}) = 0, \tag{D1}$$

where ϕ_η denotes the azimuthal angle of the emission direction $\hat{\eta}$.

The second equation can be reduced to

$$\boldsymbol{B} \cdot \nabla(\boldsymbol{r} \cdot \boldsymbol{e}) + [\boldsymbol{e} \times (\boldsymbol{B} \cdot \nabla)\boldsymbol{e}]_z / \left(1 - e_z^2\right) = 0. \tag{D2}$$

Note that the emission direction depends only on the direction of the magnetic field, but not its strength. Therefore, the only variable left is the direction of the field, which has 2 degrees of freedom. The above are two independent equations for $\boldsymbol{B}$. Therefore, the direction of $\boldsymbol{B}$ can be uniquely determined from Equations (D1), if initial condition is given. Nevertheless, the equations above are still too complicated to solve analytically. Instead of solving the equations directly, we test certain field geometries to see if the stagnation condition is satisfied.

We consider the split monopole field (Equation (B1)) and show that it does indeed satisfy Equations (D1). According to Equation (C1), the emission direction from the split monopole is exactly along the radial direction $\boldsymbol{e}^m = \boldsymbol{e}_r$. Since the strength f_0/r^2 and sign $\eta(r, \theta, \phi)$ have nothing to do with the emission direction $\boldsymbol{e}^m$, we can safely omit it in the calculations below.

Now we substitute the split monopole field into these conditions. The first equation in Equation (D1) becomes $\boldsymbol{B}^m \cdot \nabla \cos\theta = 0$. Note that $B^m_\theta = 0$; therefore, this condition is satisfied. For Equation (D2), the first term is just $B_r = 1$, while the second term can be shown to be equal to $-R \sin\theta / r(1 - \sin^2\theta) = -1$, and they sum to zero. Therefore, emission from any *one* field line in the split monopole field is projected exactly to the same point on the sky map.

Obviously, the split monopole is not the only possible solution to Equations (D1). It only corresponds to a special initial condition. In fact, we see in Figure 8 that at $r_{\rm ov} = 0.9$, SMS starts to develop from inside the LC, where the FF field still deviates from the split monopole solution. Nevertheless, SMS is much easier to achieve at smaller $r_{\rm ov}$ (see Figure 10), or at larger radii ($R \gg R_{\rm LC}$). The fact that the FF solution approaches the inclined split monopole asymptote (Bogovalov 1999), as well as the observation of SMS strongly suggest its connection to the split monopole field geometry at large radii.

REFERENCES

Abdo, A. A., et al. 2008, Science, 322, 1218
Abdo, A. A., et al. 2009a, ApJ, 695, L72
Abdo, A. A., et al. 2009b, ApJ, 696, 1084
Abdo, A. A., et al. 2009c, ApJ, 699, L102
Abdo, A. A., et al. 2009d, ApJ, 699, 1171
Abdo, A. A., et al. 2009e, ApJ, 700, 1059
Abdo, A. A., et al. 2009f, Science, 325, 840
Abdo, A. A., et al. 2009g, Science, 325, 848
Abdo, A. A., et al. 2010, ApJS, 187, 460
Arons, J. 1983, ApJ, 266, 215
Arons, J. 2008, in Neutron Stars and Pulsars, 40 Years After the Discovery, ed. W. Becker & H. H. Huang (MPE Rep. 291; Garching: MPE)
Arons, J., & Scharlemann, E. T. 1979, ApJ, 231, 854
Bai, X.-N., & Spitkovsky, A. 2010, ApJ, 715, 1270
Bogovalov, S. V. 1999, A&A, 349, 1017
Cheng, K. S., Ho, C., & Ruderman, M. 1986a, ApJ, 300, 500
Cheng, K. S., Ho, C., & Ruderman, M. 1986b, ApJ, 300, 522
Cheng, K. S., Ruderman, M., & Zhang, L. 2000, ApJ, 537, 964
Contopoulos, I., & Kalapotharakos, C. 2010, MNRAS, 381
Contopoulos, I., Kazanas, D., & Fendt, C. 1999, ApJ, 511, 351
Daugherty, J. K., & Harding, A. K. 1982, ApJ, 252, 337
Daugherty, J. K., & Harding, A. K. 1996, ApJ, 458, 278
Davis, L., & Goldstein, M. 1970, ApJ, 159, L81
Deutsch, A. J. 1955, Ann. Astrophys., 18, 1
Du, Y.-J., Qiao, G. J., Han, J. L., Lee, K. J., & Xu, R. X. 2010, MNRAS, in press, arXiv:1004.3213
Dyks, J., Harding, A. K., & Rudak, B. 2004, ApJ, 606, 1125
Dyks, J., & Rudak, B. 2003, ApJ, 598, 1201
Goldreich, P. 1970, ApJ, 160, L11
Goldreich, P., & Julian, W. H. 1969, ApJ, 157, 869
Grøn, Ø. 1984, Int. J. Theor. Phys., 23, 441
Gruzinov, A. 2005, Phys. Rev. Lett., 94, 021101
Gruzinov, A. 2006, ApJ, 647, L119
Gruzinov, A. 2007a, ApJ, 667, L69
Gruzinov, A. 2007b, arXiv:0710.1875
Gruzinov, A. 2008a, J. Cosmol. Astroparticle Phys., JCAP11(2008)002
Gruzinov, A. 2008b, arXiv:0802.1716
Gurevich, A., Beskin, V., & Istomin, Y. 1993, in Physics of the Pulsar Magnetosphere, ed. A. Gurevich, V Beskin, & Y. Istomin (Cambridge: Cambridge Univ. Press), 432
Halpern, J. P., et al. 2008, ApJ, 688, L33
Harding, A. K., Stern, J. V., Dyks, J., & Frackowiak, M. 2008, ApJ, 680, 1378
Harding, A. K., Tademaru, E., & Esposito, L. W. 1978, ApJ, 225, 226
Hirotani, K. 2007, ApJ, 662, 1173
Kalapotharakos, C., & Contopoulos, I. 2009, A&A, 496, 495
Kirk, J. G., Skjæraasen, O., & Gallant, Y. A. 2002, A&A, 388L, 29
Komissarov, S. S. 2006, MNRAS, 367, 19
Lyubarskii, Y. E. 1996, A&A, 311, 172
Lyubarsky, Y. 2008, in AIP Conf. Ser. 983, 40 Years of Pulsars: Millisecond Pulsars, Magnetars and More, ed. C. Bassa, Z. Wang, A. Cumming, & V. M. Kaspi (Melville, NY: AIP), 29
Lyubarsky, Y. 2009, ApJ, 696, 320
Lyutikov, M., & Thompson, C. 2005, ApJ, 634, 1223
McKinney, J. C. 2006, MNRAS, 368, L30
Melatos, A. 2000, MNRAS, 313, 217
Michel, F. C. 1973a, ApJ, 180, 207
Michel, F. C. 1973b, ApJ, 180, L133
Muslimov, A. G., & Harding, A. K. 2003, ApJ, 588, 430
Muslimov, A. G., & Harding, A. K. 2004, ApJ, 606, 1143
Pellizzoni, A., et al. 2009a, ApJ, 691, 1618
Pellizzoni, A., et al. 2009b, ApJ, 695, L115
Pétri, J. 2009, A&A, 503, 13
Pétri, J., & Kirk, J. G. 2005, ApJ, 627, L37
Qiao, G.-J., Lee, K.-J., Wang, H.-G., Xu, R.-X., & Han, J. L. 2004, ApJ, 606, L49
Qiao, G.-J., Lee, K.-J., Zhang, B., Wang, H.-G., & Xu, R.-X. 2007, Chin. J. Astron. Astrophys., 7, 496
Rafikov, R. R., & Goldreich, P. 2005, ApJ, 631, 488
Romani, R. W., & Yadigaroglu, I.-A. 1995, ApJ, 438, 314
Schiff, L. I. 1939, Proc. Natl. Acad. Sci., 25, 391
Spitkovsky, A. 2006, ApJ, 648, L51
Spitkovsky, A. 2008, in AIP Conf. Ser. 983, 40 Years of Pulsars: Millisecond Pulsars, Magnetars and More, ed. C. Bassa, Z. Wang, A. Cumming, & V. M. Kaspi (Melville, NY: AIP), 20
Takata, J., & Chang, H.-K. 2007, ApJ, 670, 677
Takata, J., Chang, H.-K., & Cheng, K. S. 2007, ApJ, 656, 1044
Takata, J., Chang, H.-K., & Shibata, S. 2008, MNRAS, 386, 748
Tang, A. P. S., Takata, J., Jia, J. J., & Cheng, K. S. 2008, ApJ, 676, 562
Thompson, D. J. 2004, in Astrophysics and Space Science Library 304, Cosmic Gamma-Ray Sources, ed. K. S. Cheng & G. E. Romero (Dordrecht: Kluwer), 149
Timokhin, A. N. 2006, MNRAS, 368, 1055
Timokhin, A. N. 2007a, Ap&SS, 308, 575
Timokhin, A. N. 2007b, MNRAS, 379, 605
Venter, C., Harding, A. K., & Guillemot, L. 2009, ApJ, 707, 800
Watters, K. P., Romani, R. W., Weltevrede, P., & Johnston, S. 2009, ApJ, 695, 1289
Weltevrede, P., & Johnston, S. 2008, MNRAS, 391, 1210
Yadigaroglu, I.-A. G. 1997, PhD thesis, Stanford Univ.